

Deployment and evaluation of an $\text{NH}_4^+/\text{H}_3\text{O}^+$ reagent-ion switching chemical ionization mass spectrometer for the detection of reduced and oxygenated gas-phase organic compounds

Cort L. Zang¹ and Megan D. Willis¹

¹Department of Chemistry, Colorado State University, Fort Collins, CO, USA

Correspondence: Megan D. Willis (megan.willis@colostate.edu)

Abstract. Reactive organic carbon (ROC) is diverse in its speciation, functionalization, and volatility, with varying implications for ozone production and secondary organic aerosol formation and growth. Chemical ionization mass spectrometry (CIMS) approaches can provide in situ ROC observations and the CIMS reagent-ion controls the detectable ROC species. To expand the range of detectable ROC, we describe a method for switching between the reagent-ions NH_4^+ and H_3O^+ in a Vocus chemical ionization time-of-flight mass spectrometer (Vocus-CI-ToFMS). We describe optimization of ion-molecule reactor conditions for both reagent-ions, at the same temperature, and compare the ability of NH_4^+ and H_3O^+ to detect a variety of volatile organic compounds (VOCs), semi-volatile, and intermediate volatility organic compounds (S/IVOCs) including oxygenates and organic sulfur compounds. Sensitivities are comparable to other similar instruments (up to ~ 5 counts s^{-1} ppt_v^{-1}) with detection limits on the order of 1-10 s of ppt_v (1 s integration time). We report a method for characterizing and filtering periods of hysteresis following each reagent-ion switch and compare use of reagent-ions, persistent ambient ions, and a deuterated internal standard for diagnosing this hysteresis. We deploy $\text{NH}_4^+/\text{H}_3\text{O}^+$ reagent-ion switching in a rural pine forest in central Colorado, US, and ~~report a method for characterizing and filtering periods of hysteresis following each reagent-ion switch.~~ We use our ambient measurements to compare the capabilities of NH_4^+ and H_3O^+ in the same instrument, without interferences from variation in instrument and inlet designs. We find that H_3O^+ optimally detects reduced ROC species with high volatility, while NH_4^+ improves detection of functionalized ROC compounds, including organic nitrates and oxygenated S/IVOCs that are readily fragmented by H_3O^+ .

1 Introduction

Tropospheric aerosol formation, oxidant reactivity, and ozone production are driven by the molecularly diverse pool of atmospheric reactive organic carbon (ROC; all organic species excluding methane) (Heald and Kroll, 2020). Speciation of atmospheric ROC is an ongoing analytical challenge (e.g., Goldstein and Galbally, 2007; Hunter et al., 2017), especially at time resolutions relevant to atmospheric mixing and chemistry. While reduced volatile organic compounds (VOCs, with saturation vapor concentration, C^* , $> 3 \times 10^6 \mu\text{g m}^{-3}$) are an important fraction of ROC, functionalized species with lower volatility (semi-volatile and intermediate volatility organic compounds, S/IVOCs with C^* between 0.3 and $3 \times 10^6 \mu\text{g m}^{-3}$) are major contributors to ozone production and aerosol formation (e.g., Xu et al., 2021; Heald and Kroll, 2020; Bianchi et al., 2019; Don-

25 ahue et al., 2011). For example, near comprehensive measurements of ROC at a forested site showed that S/IVOCs contribute approximately one third of ·OH-reactivity and potential secondary organic aerosol production (Hunter et al., 2017). Further, semi-volatile and oxygenated VOCs contribute to marine secondary aerosol formation (Burkart et al., 2017; Mungall et al., 2017; Croft et al., 2019, 2021), and oxygenated species such as furans contribute significantly to ·OH-reactivity and aerosol production in wildfire plumes (Xu et al., 2021). In many urban environments, volatile chemical products and other classes of IVOCs make a growing contribution to aerosol and ozone production (Coggon et al., 2021; Zhao et al., 2014b). However, owing to limitations in analytical techniques, and partitioning to inlet and instrument surfaces (Deming et al., 2019; Pagonis et al., 2019), oxygenated and otherwise functionalized S/IVOCs are often unmeasured.

Chemical ionization mass spectrometry (CIMS) represents a family of analytical techniques applied to detect and characterize organic and inorganic trace gases in whole air at high time resolution (e.g., Zhang et al., 2023; Yuan et al., 2017; Huey, 2007). The choice of reagent-ion determines the scope of the measurement in terms of ROC functionality and chemistry, while instrument construction and design impacts the range of detectable species in terms of volatility and reactivity (e.g., Riva et al., 2019; Krechmer et al., 2018). A range of reagent-ions are in common use and are selective toward specific ROC classes. Oxygenated, multi-functional organic gases can be detected as negative ions using iodide ($I^-/(H_2O)_n \cdot I^-$) (Lee et al., 2018, 2014), acetate ($CH_3CO_2^-$) (Brophy and Farmer, 2015; Roberts et al., 2010), CF_3O^- (Crouse et al., 2013, 2006), sulfur hexafluoride (SF_6^-) (Nah et al., 2018; Huey, 2007), nitrate (NO_3^-) and bromide (Br^-) (Rissanen et al., 2019; Bianchi et al., 2019) reagent-ions. Highly oxygenated organic species (with $C^* < 0.3 \times 10^6 \mu g m^{-3}$), together with low volatility inorganic species (e.g., H_2SO_4), can be detected with nitrate and bromide ionization at ambient pressure (Bianchi et al., 2019; Rissanen et al., 2019; Riva et al., 2019). CF_3O^- effectively detects organic peroxides (Crouse et al., 2013, 2006), while I^- , Br^- , NO_3^- and SF_6^- detect a range of polar and acidic gases (Riva et al., 2019; Lee et al., 2018, 2014). Reduced VOCs, small oxygenated VOCs (e.g., methanol, ethanol, acetone, acetaldehyde) and reduced sulfur compounds (e.g., dimethyl sulfide and methanethiol) are readily detected as positive ions via proton transfer with hydronium (H_3O^+) reagent-ions (e.g., Kilgour et al., 2022; Pagonis et al., 2019; Krechmer et al., 2018; Yuan et al., 2017). NO^+ and O_2^+ allow detection of reduced VOCs, with proton affinities below that of water, that are generally not detectable with H_3O^+ (Jordan et al., 2009; Smith and Spanel, 2005). While H_3O^+ can detect functionalized VOCs, fragmentation is common and complicates the interpretation of mass spectra from complex samples (e.g., Coggon et al., 2024; Kilgour et al., 2024; Li et al., 2021; Pagonis et al., 2019; Yuan et al., 2017). To overcome some of the limitations induced by H_3O^+ ionization, fast separation techniques have been coupled to proton-transfer instruments (Claflin et al., 2021; Stockwell et al., 2021; Vermeuel et al., 2023b; Coggon et al., 2024; Kilgour et al., 2024), and other positive polarity reagent-ions have been applied to functionalized ROC. Benzene ($C_6H_6^+$) reagent-ions detect dimethyl sulfide, monoterpenes and sesquiterpenes with reduced fragmentation and higher selectivity compared to H_3O^+ (Kim et al., 2016). Water clusters (i.e., $(H_2O)_nH^+$) can detect a small subset of species detected by H_3O^+ , such as dimethyl sulfide, with high selectivity (Blomquist et al., 2010). An array of oxygenated, multi-functional compounds in the intermediate to semi-volatile range can be detected using ammonium reagent-ions (e.g., Xu et al., 2022; Khare et al., 2022; Muller et al., 2020; Hansel et al., 2018), which provide some overlap in the fractions of ROC detected by negative polarity reagent-ions such as I^- and CF_3O^- .

Compared to other positive polarity reagent-ions, ammonium (NH_4^+) adduction ionization is selective toward a wider range of multi-functional oxygenated compounds, such as carbonyls, alcohols, ethers, furans, and siloxanes (Xu et al., 2022; Khare et al., 2022; Muller et al., 2020; Zhang et al., 2019; Zaytsev et al., 2019a; Berndt et al., 2019). Ambient observations have recently shown that NH_4^+ ionization can detect organic nitrates (Xu et al., 2022), while laboratory studies have demonstrated detection of organic peroxides (Zhou et al., 2018) and peroxy radicals (Hansel et al., 2018). Selected ion flow tube mass spectrometry (SIFT-MS) studies show that NH_4^+ ions form the strongest associations with carbonyl groups, relative to other oxygenates (e.g., alcohols and ethers) (Adams 2003). However, the conditions under which reagent-ions form and ion-molecule reactions occur determine the dominant reagent-ion and ionization mechanism, which in turn controls the scope of detectable compounds and associated sensitivity. Possible reagent-ions include $\text{NH}_4 \cdot \text{X}_n^+$ (where $\text{X} = \text{H}_2\text{O}$ or NH_3 and $n = 0, 1, 2, \dots$). In practice, multiple reagent-ions can be present, with $\text{NH}_4 \cdot \text{H}_2\text{O}^+$ providing optimal sensitivity to oxygenated compounds (Xu et al., 2022). Reactions with neutral analytes occur through ligand switching (Reaction R1), where the evaporation of X promotes softer adduct formation compared to NH_4^+ alone (i.e., $n = 0$) (Xu et al., 2022; Canaval et al., 2019; Adams et al., 2003).



Given an analyte, A, with larger NH_4^+ affinity (i.e., the negative enthalpy of the reaction: $\text{NH}_4^+ + \text{A} \rightarrow \text{A} \cdot \text{NH}_4^+$; e.g., Xu et al. (2022)) than X, the ionization reaction (R1) is exothermic (Adams et al., 2003). Therefore, $\text{NH}_4 \cdot \text{X}^+$ ligand switching reactions will proceed efficiently at or near the collision limit, with little importance of the reverse reaction unless reaction timescales are long or the reaction is endothermic or only slightly exothermic (Xu et al., 2022; Zaytsev et al., 2019a). Reaction R1 is exothermic for the majority of oxygenates and multi-functional compounds (Xu et al., 2022; Adams et al., 2003; Canaval et al., 2019; Zaytsev et al., 2019a) (~~Table S1, Edward P. Hunter and Sharon G. Lias; Michael M. Meot-Ner (Mautner) and Sharon G. Lias~~) (Table S3, Edward P. Hunter and Sharon G. Lias; Michael M. Meot-Ner (Mautner) and Sharon G. Lias); however, ion-molecule reactor (IMR) conditions must be selected to promote pure ion chemistry, optimize sensitivity, and minimize fragmentation.

Many CIMS reagent-ions provide access to complementary fractions of ambient ROC, and combining multiple reagent-ions in a single CIMS instrument can provide several advantages. First, reagent-ion switching can maintain the benefits of selectivity afforded by specific reagent-ions, while expanding the number of detectable compounds. For example, H_3O^+ and NO^+/O_2^+ are combined in proton-transfer reaction (PTR) and SIFT-MS instruments to expand detection capabilities to a broad range of alkanes, alkenes, aromatics, and some oxygenated species (e.g., Agarwal et al., 2014; Smith and Spangel, 2005). Further, the combination of nitrate and bromide reagent-ions allows detection of a wide range of highly oxygenated molecules along with hydroperoxyl radicals, iodine compounds and sulfuric acid (He et al., 2023; Rissanen et al., 2019). Iodide, acetate and water cluster reagent-ions have been combined in laboratory studies, using repeated experiments rather than active reagent switching, to expand the range of detectable ROC (Aljawhary et al., 2013) and inform development of reaction mechanisms (e.g., Zhao et al., 2014a). Thus, combining reagent-ions can decrease the potentially large number of instruments required to characterize a broad range of ROC classes (e.g., Heald and Kroll, 2020). Second, combining reagent-ions in a single instrument allows for direct comparison between the fractions of ROC detected by each chemical ionization reagent (e.g., Zaytsev et al., 2019a).

For example, rapid switching between iodide and the acid-selective acetate reagent-ion informs detection of organic acids with iodide (e.g., Brophy and Farmer, 2015). Switching between NH_4^+ and H_3O^+ has benefits for measuring both reduced VOCs and their early generation oxidation products (Zaytsev et al., 2019a, b), while also allowing a direct comparison between the subsets of ROC detected by each reagent-ion without the complications associated with differing instrument and inlet design (e.g., Riva et al., 2019).

Ambient atmospheric observations with NH_4^+ adduct ionization CIMS have focused primarily on urban environments, where NH_4^+ ion chemistry allows detection of oxygenated VOCs from volatile chemical products (Xu et al., 2022; Khare et al., 2022). $\text{NH}_4^+/\text{H}_3\text{O}^+$ reagent-ion switching has so far been limited to laboratory experiments demonstrating feasibility of switching (Muller et al., 2020) and application following laboratory oxidation of VOCs and oxygenated VOCs (Zaytsev et al., 2019a, b). We characterize $\text{NH}_4^+/\text{H}_3\text{O}^+$ reagent-ion switching using a Vocus Chemical Ionization Time-of-Flight Mass Spectrometer (Vocus-CI-ToFMS) using both laboratory standards and deployment at a rural forested site. We describe selection of ideal IMR conditions for $\text{NH}_4^+/\text{H}_3\text{O}^+$ reagent-ion switching, at the same temperature, with a focus on sensitivity, fragmentation, and prominence of competing ionization pathways. Using ambient reagent-ion switching data, we describe an approach to filter periods of impure ion chemistry, and once filtered, ambient observations allow us to directly compare the fractions of ambient ROC detected by H_3O^+ and NH_4^+ . Our observations demonstrate that NH_4^+ is able to detect oxygenated and multi-functional biogenic ROC with both reduced fragmentation and higher selectivity compared to H_3O^+ , illustrating a highly complimentary set of CIMS reagent-ions.

2 Methods and field site description

2.1 Instrument description

The Vocus-CI-ToFMS ([Vocus-S](#), Tofwerk AG and Aerodyne Research Inc.) is described in detail elsewhere (Krechmer et al., 2018), with a brief description supplied here. Two features differentiate the Vocus-CI-ToFMS from other chemical ionization or proton transfer reaction time-of-flight mass spectrometers. First, the Vocus-CI-ToFMS is equipped with a focusing ion-molecule reactor (fIMR) which consists of a radio-frequency only quadrupole oriented around a 10 cm long resistive glass tube (Krechmer et al., 2018). The fIMR focuses ions toward the center-line, reducing ion losses to the walls and promoting ion transmission into a quadrupole high pass mass filter (BSQ). Second, polyether ether ketone (PEEK) tubing is used to establish flow restriction between ambient pressure and the fIMR. The use of PEEK at the instrument inlet reduces interactions between sampled air and more absorptive surfaces which impact transmission of S/IVOCs into the fIMR (Deming et al., 2019). These modifications to the Vocus-CI-ToFMS improve the ability to detect both reduced and oxidized ROC (Riva et al., 2019). The Vocus-CI-ToFMS used in this study has a mass resolving power of ~ 5000 m dm^{-1} , a mass range of ~ 50 -500 m/z , with a 25 kHz ToF extraction frequency and is equipped with a multi-port reagent-ion injection, current-regulated discharge ion source. [Details about instrument voltages are available in Table S1.](#)

[When using \$\text{H}_3\text{O}^+\$ ionization, we inject \$20 \text{ cm}^3 \text{ min}^{-1}\$ \(STP\) from the head-space above ultra high purity water \(MilliporeSigma, OmniSolv LC-MS\) under vacuum into the discharge ion source. When switching to \$\text{NH}_4^+\$ ionization, we further add a flow](#)

130 from the head-space above a ~ 1 w/w% solution of ammonium hydroxide (Oakwood Products Inc., Trace Metals Grade) in water to the ion source. Additionally, when switching between reagent-ions the voltages and pressure in the fIMR and the ion optics are adjusted to compliment each reagent-ion, taking into account sensitivity, fragmentation, and purity of ionization chemistry; this is discussed in Sect. 3.1. A change between ionization modes results in hysteresis where the ion chemistry is impure. The filtering of hysteretic periods is discussed in Sect. 3.4.

2.2 Reactor pressure and voltage gradient

The fIMR collision energy can be controlled in part by adjusting the conditions that impact the velocity, free path, and thermal energy of ions; axial voltage gradient, pressure, and temperature. The temperature must remain constant during reagent-ion switching to allow for switching on 15-minute timescales. This restricts control of collisional energy to adjustments of the fIMR voltage gradient and pressure. To understand the impact that these parameters have on ion chemistry, we introduce a constant flow of dilute calibration standard while systematically changing the fIMR voltage gradient and pressure. We change the fIMR pressure in 0.1 mbar increments and hold it constant while we increase the fIMR front voltage by 10 V steps. With NH_4^+ , we characterized from 2.5 to 3.5 mbar and from 45 to 65 Vcm^{-1} (60-120 Townsends (Td)). For H_3O^+ , we characterized from 1.5 to 2.5 mbar and from 45 to 65 Vcm^{-1} (80-200 Td).

140 2.3 Sensitivity, detection limit, and fragmentation with standards

We calibrated 23 analytes from multi-component standardized gas cylinders (Apel-Riemer Environmental Inc.) to report sensitivities ($\text{counts s}^{-1} \text{ppt}_v^{-1}$) and detection limits (3σ of the background with 1s integration). The 23 analytes come from three separate multi-component cylinders where the composition was selected to avoid interferences from fragments (Table S2). Backgrounds were obtained using a zero air generator (Sabio Model 1001). We investigate fragmentation of molecular ions using single component samples of trans-2-hexen-1-ol (96.5 %, Acros Organics, Lot: A0340603), β -cyclocitral (92.3 %, ThermoFisher, Lot: 10237632), 2-hexenal (97.5 %, Oakwood Products Inc., Lot: 098868J07I), 2-hexanone (100 %, Oakwood Products Inc., Lot: 098350R22K), and 2-methyl-3-buten-2-ol (99.5 %, Oakwood Products Inc., Lot: 051281K14H). To calculate a molecular ion fraction, we average 15 s of 2 Hz data and fit peaks corresponding to molecular ions (i.e., $\text{A} \cdot \text{H}^+$ for H_3O^+ and $\text{A} \cdot \text{NH}_4^+$ for NH_4^+), identified fragments, and clusters then divide the molecular ion signal by the sum of all related peaks. fIMR conditions for H_3O^+ ionization during these experiments were 2.2 mbar, 60 °C, with a voltage gradient of 67.5 Vcm^{-1} and (140 Td) and a BSQ amplitude of 270 V. Using a 60 °C reaction chamber with H_3O^+ is lower than commonly reported in the literature (~ 80 -100 °C) (e.g., Vermeuel et al., 2023a; Coggon et al., 2024); this choice arises from fIMR temperature constraints for NH_4^+ (Xu et al., 2022) and is discussed in more detail in Sect. 3.1. For NH_4^+ ionization the fIMR settings were 3.1 mbar, 60 °C, with a voltage gradient of 60 Vcm^{-1} (90 Td) and a BSQ amplitude of 250 V. The BSQ frequency was 2.2 MHz, and the fIMR amplitude and frequency were 500V and 1.6 MHz respectively (Table S1).

2.4 Signal response to ambient relative humidity

To test the effect of relative humidity on sensitivity we varied the ratio of wet and dry flows (controlled with mass flow controllers, MKS Instruments Model 1179C Mass-Flo) to achieve a range of relative humidities. The relative humidity was measured inline (Omega Engineering Model HX71-V1). Downstream of the relative humidity measurement $10 \text{ cm}^3 \text{ min}^{-1}$ (STP) of a certified gas standard (Apel-Riemer Environmental Inc. and Airgas for dimethyl sulfide) was added to the humidified flow before being sampled to the Vocus-CI-ToFMS. Relative humidity ranged between 15 and 85 % during the experiments. Measurements alternated between elevated relative humidity and dry conditions, such that each measurement at elevated humidity could be directly compared to a dry (0 % RH) measurement immediately before.

2.5 Observations at Manitou experimental forest observatory

We deployed a Vocus-CI-ToFMS in Manitou Experimental Forest Observatory (MEFO) from September 3rd to September 24th of 2021. MEFO is a rural ponderosa pine forest at middle elevation ($\sim 2,300 \text{ m}$) located $\sim 40 \text{ km}$ northwest of Colorado Springs and $\sim 70 \text{ km}$ southwest of Denver (39.1006°N , 105.0942°W). The ROC composition at this site is well characterized with emissions dominated by local biogenic sources (Hunter et al., 2017; Vermeuel et al., 2023a; Riches et al., 2024; Link et al., 2024). A full description of the field site can be found in Ortega et al. (2014). The Vocus-CI-ToFMS sample inlet was $\sim 4 \text{ m}$ of 0.25 inch outer diameter perfluoroalkoxy (PFA) tubing situated $\sim 4 \text{ m}$ above ground. The inlet flow was $\sim 3.8 \text{ L min}^{-1}$ (i.e., 2.9 L min^{-1} (STP)) pulled by a flow restricted bypass pump resulting in a laminar flow inlet (Reynolds number of ~ 1150) corresponding to a residence time of $\sim 0.7 \text{ s}$. The inlet likely produced wall loss of oxygenated ROC and while the extent was not quantified, minimizing the inlet inner diameter and maximizing the flow rate, while maintaining laminar flow, serve to minimize inlet losses and tubing delays (Pagonis et al., 2017). The Vocus-CI-ToFMS sub-sampled $93\text{-}100 \text{ cm}^3 \text{ min}^{-1}$ (i.e., $71\text{-}77 \text{ cm}^3 \text{ min}^{-1}$ (STP)) perpendicular to the main inlet flow which helps prevent ambient aerosol clogging the capillary inlet interface compared to a linear sub-sampling assembly (Jensen et al., 2023). We performed bi-hourly, 3 minute instrument backgrounds with ultra zero air (Airgas, UZA grade) followed by a 1 minute, single-point calibration with a certified calibrant mixture (Apel-Riemer Environmental Inc.) for both reagent-ions.

The Vocus-CI-ToFMS switched between NH_4^+ and H_3O^+ ionization on 15-minute time intervals during the deployment in MEFO. fMR conditions for H_3O^+ ionization were 2.5 mbar , 60°C , with a voltage gradient of 62 Vcm^{-1} and a BSQ amplitude of 350 V ; and for NH_4^+ ionization were 3.1 mbar , 60°C , with a voltage gradient of 65 Vcm^{-1} and a BSQ amplitude of 250 V . The fMR settings correspond to E/N values of 114 Td and 96 Td for H_3O^+ and NH_4^+ respectively. The BSQ frequency was 2.2 MHz , and the fMR amplitude and frequency were 450 V and 1.3 MHz respectively (Table S1). fMR parameters for both reagent-ions were informed by experiments detailed in Sect. 3.1.

2.5.1 NH_4^+ and H_3O^+ instrument conditions

~~The Vocus-CI-ToFMS switched between NH_4^+ and H_3O^+ ionization on 15-minute time intervals during the deployment in MEFO. fMR conditions for H_3O^+ ionization were 2.5 mbar , 60°C , with a voltage gradient of 62 Vcm^{-1} ; and for NH_4^+~~

ionization were 3.1 mbar, 60 °C, with a voltage gradient of 65 Vcm⁻¹. The fIMR settings correspond to E/N values of 114 Td and 96 Td for H₃O⁺ and NH₄⁺ respectively. fIMR parameters for both reagent ions were informed by experiments detailed in Sect. 3.1. When using H₃O⁺ ionization, we inject 20 cm³ min⁻¹ (STP) from the head-space above ultra-high purity water (MilliporeSigma, OmniSolv LC-MS) under vacuum into the discharge ion source. When switching to NH₄⁺ ionization, we further add a flow from the head-space above a ~1 w/w% solution of ammonium hydroxide (Oakwood Products Inc., Trace Metals Grade) in water to the ion source. Additionally, when switching between reagent ions the voltages and pressure in the fIMR and the ion optics are adjusted to compliment each reagent ion, taking into account sensitivity, fragmentation, and purity of ionization chemistry; this is discussed in Sect. 3.1. A change between ionization modes results in hysteresis, where the ion chemistry is impure, the filtering of hysteretic periods is discussed in Sect. 3.4.

2.6 ARTofMELT Expedition on icebreaker (I/B) Oden

We deployed the Vocus-CI-ToFMS on-board Swedish I/B *Oden* from May 7th to June 15th of 2023 as part of the Atmospheric Rivers and the onset of Arctic MELT measurement expedition (ARTofMELT). The cruise on I/B *Oden* took place within the pack ice and marginal ice zone between Svalbard and Greenland in the Fram Strait. The Vocus-CI-ToFMS switched between NH₄⁺ and H₃O⁺ ionization on 15-minute time intervals during the expedition. The Vocus-CI-ToFMS was mounted to the floor of a sea container on I/B *Oden*'s 4th deck using metal plates and five high deflection vibration isolation feet (Barry Controls Model 2K2-BA-90) and was mounted to an open wall using two wire rope isolators (Enidine Model WR6-850-10-E).

Ambient air was sampled through a 0.375 inch outer diameter PFA tube ~15 m in length. The entire length of tubing was insulated and heated to 30 °C in three separately controlled sections. The Vocus-CI-ToFMS inlet flow was driven by a vacuum pump (Agilent IDP-7 Dry Scroll) regulated by a mass flow controller (15 L min⁻¹ (STP)). A deuterated internal standard (containing dimethylsulfide-d₃, acetone-d₆, 2-hexanone-d₄, and mesitylene-d₁₂) was injected near the top of the Vocus-CI-ToFMS inlet through a 0.125 inch outer diameter PFA tube at a rate of 5 cm³ min⁻¹ (STP) into the total inlet flow of 15 L min⁻¹ (STP) yielding ~333 ppt_v from the nominally 1 ppm standardized cylinder (Apel-Riemer Environmental Inc.). The inlet assembly was affixed to a metal pipe extending from the top of the sea container toward the bow of the ship at a ~40° angle ~3 m above the top of the container or 25 m above the water/ice surface. The use of internal standards during this expedition allows us to analyze reagent-ion hysteresis (Sect. 3.4) using a persistent and known set of ions. fIMR conditions for H₃O⁺ ionization during ARTofMELT were 2.2 mbar, 60 °C, a voltage gradient of 67.5 Vcm⁻¹ (140 Td) and a 270 V BSQ amplitude. For NH₄⁺ ionization the fIMR settings were 3.1 mbar, 60 °C, a 60 Vcm⁻¹ (90 Td) voltage gradient, and a 250 V BSQ amplitude. The BSQ frequency was 2.2 MHz, and the fIMR amplitude and frequency were 500V and 1.6 MHz respectively (Table S1) We reserve further analysis of the ARTofMELT data set for future work.

2.7 Data analysis

Raw mass spectra spectral data were collected with Acquity (version 2.3.18) and ToFDAQ (version 1.99) (Tofwerk AG) and processed in Tofware (version 3.2.5, Tofwerk AG and Aerodyne Research Inc.). For MEFO data, the time resolution was pre-averaged from 1 Hz to 0.1 Hz. For ARTofMELT data, the time resolution was pre-averaged from 2 Hz to 1 Hz. All data

was mass calibrated, baseline subtracted, and peak fit in Tofware. Time-integrated high resolution ion signals were exported for further analysis in python (version 3.9.12). Responses in the E/N scans in Sect. 3.1 were interpolated using a linear interpolation on a triangular grid (using `matplotlib.tri.LinearTriInterpolator`). C^* values are estimated using EPI Suite (US EPA).

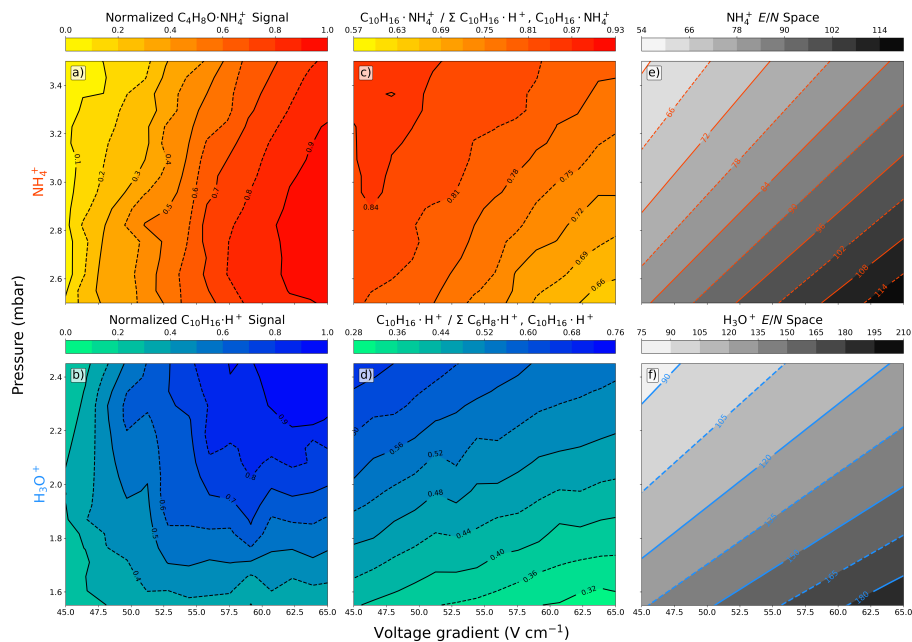


Figure 1. (a-d) Contour plots of fIMR pressure and voltage gradient scans with a constant concentration of analyte (10 ppb_v) introduced into the Vocus-CI-ToFMS. Normalized signal intensity for (a) methyl ethyl ketone measured with NH₄⁺ (C₄H₈O · NH₄⁺) and (b) α-pinene measured with H₃O⁺ (C₁₀H₁₆ · H⁺). (c) Fractional contribution of the NH₄⁺ molecular ion (C₁₀H₁₆ · NH₄⁺) to the total α-pinene signal (i.e., the sum of the proton transfer product (C₁₀H₁₆ · H⁺) and the molecular ion). (d) Fractional contribution of the H₃O⁺ molecular ion (C₁₀H₁₆ · H⁺) to the total α-pinene signal (i.e. the sum of the α-pinene fragment (C₆H₈ · H⁺) and the molecular ion). Contour plots of calculated *E/N* values over the scanned space for both (e) NH₄⁺ and (f) H₃O⁺.

3.1 Ion-molecule reactor pressure and voltage gradient

H_3O^+ and NH_4^+ ionization operate optimally at differing combinations of fIMR pressure, voltage gradient, and temperature (Xu et al., 2022; Gouw and Warneke, 2007), all of which impact the reduced electric field (E/N) of the fIMR:

$$E/N = \frac{T \times \Delta V \times k_B}{l_{\text{fIMR}} \times p} \quad (1)$$

230 Where T is the temperature (kelvin), ΔV is the difference between the front and back voltage (volts), l_{fIMR} is the fIMR length (meters), k_B is the Boltzmann constant (joules per kelvin), and p is pressure (pascals or joules per cubic meter). E/N has units of townsend (Td, $1 \text{ Td} = 1 \times 10^{-17} \text{ Vcm}^2$) and describes ion velocity and collisional energy. High E/N values promote increased fragmentation and reduced clustering while low E/N values promote cluster formation and reduced fragmentation. We analyzed relative sensitivity, fragmentation, and prevalence of ionization pathways, while varying the fIMR pressure and voltage gradient with a constant temperature of 60°C (Fig. 1) to inform our selection of fIMR settings. Because fIMR temperature takes tens of minutes to stabilize, we selected a constant 60°C fIMR temperature to promote $\text{NH}_4^+ \cdot \text{H}_2\text{O}$ clusters in NH_4^+ ionization. This is lower than most H_3O^+ fIMR temperatures ($\sim 80\text{-}100^\circ\text{C}$), however, the effect of lower fIMR temperature on the reagent-ion distribution can be mitigated by adjusting other fIMR settings.

Selecting H_3O^+ ionization fIMR parameters requires balancing fragmentation and sensitivity. We observe a large increase 240 ($>60\%$ at 2.4 mbar) in the sensitivity to the molecular ion ($\text{C}_{10}\text{H}_{16} \cdot \text{H}^+$) with increased fIMR voltage gradient (Fig. 1b) which arises from three main factors. First, reduced residence time with increased voltage gradient ($163 \mu\text{s}$ or $113 \mu\text{s}$ at 45 Vcm^{-1} or 65 Vcm^{-1} respectively with pressure and temperature of 2.4 mbar and 333.15 K) could increase ion transmission through the fIMR. Second, at low E/N protonated water clusters contribute to the ionization of α -pinene. The production of protonated water clusters is evident from the reduced benzene sensitivity at lower E/N (Fig. A1) (Gouw and Warneke, 2007). 245 Water clusters have a higher proton affinity (i.e., the negative enthalpy of the reaction: $\text{H}^+ + \text{A} \rightarrow \text{A} \cdot \text{H}^+$) compared to water (Hunter and Lias, 1998), and α -pinene has a higher proton affinity than both water and the first water cluster (i.e., $(\text{H}_2\text{O})_2$), making ionization reactions with both exothermic. In contrast, benzene has a proton affinity higher than water but lower than the first cluster, making the ionization reaction of benzene with $(\text{H}_2\text{O})_2\text{H}^+$ endothermic and unlikely. Therefore the formation of water clusters will reduce the sensitivity to benzene while increasing the sensitivity to α -pinene. Third, the known H_3O^+ 250 α -pinene fragment, $\text{C}_6\text{H}_8 \cdot \text{H}^+$ has a larger contribution to the total α -pinene signal at higher E/N (Fig. 1d) which suggests that part of the increased sensitivity to $\text{C}_{10}\text{H}_{16} \cdot \text{H}^+$ at higher pressures is also attributable to reduced loss to fragmentation. The combined responses of transmission, fragmentation, and proton affinity to changes in voltage and pressure with H_3O^+ ionization result in a sensitivity that does not follow E/N directly (Fig. 1b & 1f).

Selecting NH_4^+ ionization fIMR parameters requires balancing between signal intensity and purity of ion chemistry. Similar 255 to H_3O^+ , with NH_4^+ we observe increased signal intensity of the methyl ethyl ketone molecular ion ($\text{C}_4\text{H}_8\text{O} \cdot \text{NH}_4^+$) at higher voltage gradients (Fig. 1a). In contrast to α -pinene detection with H_3O^+ , sensitivity to $\text{C}_4\text{H}_8\text{O} \cdot \text{NH}_4^+$ is not impacted by fragmentation and changing reagent-ion proton affinity across the range in voltage gradient. The sensitivity to the $\text{C}_4\text{H}_8\text{O} \cdot \text{NH}_4^+$

ion is highest at high E/N , but the change in sensitivity is mostly dependent on the voltage gradient and is less impacted by the FIMR pressure (Fig. 1a). We observe a similar trend for other oxygenated ROC species (Fig. A2). The vertical contours in the NH_4^+ sensitivity contrasted with the L-shaped contouring in the H_3O^+ sensitivity (Fig. 1a & 1b) supports the three-factor dependence for H_3O^+ on transmission, fragmentation, and proton affinity, and points to transmission as the major factor impacting sensitivity with NH_4^+ ionization. However, at high E/N we observe impurities in the ionization chemistry (i.e., proton transfer products ($\text{A} \cdot \text{H}^+$) occurring for α -pinene) with NH_4^+ ionization (Fig. 1c). Proton transfer ionization under NH_4^+ is undesirable because it provides lower selectivity, leads to higher fragmentation rates compared to the ligand-switching mechanism, and complicates interpretation of the mass spectrum. α -pinene has a lower ammonium affinity than H_2O (Canaval et al., 2019) which makes the ligand switching reaction (R1) endothermic and thus dependent on increased collisional energy at higher voltage gradients (Xu et al., 2022). We observe a larger contribution of the proton transfer product at higher E/N , which is consistent with electric field-induced production of $\text{C}_{10}\text{H}_{16} \cdot \text{H}^+$ through internal proton transfer (Xu et al., 2022). Alternatively, it is also possible that $\text{C}_{10}\text{H}_{16} \cdot \text{H}^+$ production is enhanced by declustering of the $\text{NH}_4^+ \cdot \text{H}_2\text{O}$ ions to form NH_4^+ which is more likely to undergo proton transfer reactions directly, without the need for internal proton transfer, due to the lower proton affinity of NH_3 compared to α -pinene (Canaval et al., 2019). Regardless of the mechanism, formation of proton transfer products is ideally avoided and we find that their production is minimized at low E/N (Fig. 1c). We note that the formation of secondary clusters (i.e., $\text{NH}_4 \cdot \text{H}_2\text{O} \cdot \text{A}^+$ and $\text{NH}_4 \cdot \text{NH}_3 \cdot \text{A}^+$) is negligible over the entire investigated E/N space (Fig. S1 & S2). The sensitivity to methyl ethyl ketone, and prevalence of undesirable reaction products ($\text{C}_{10}\text{H}_{16} \cdot \text{H}^+$) are optimal under opposing conditions in the voltage gradient-pressure space, such that optimal FIMR parameters for NH_4^+ require a compromise between sensitivity and purity of ionization chemistry.

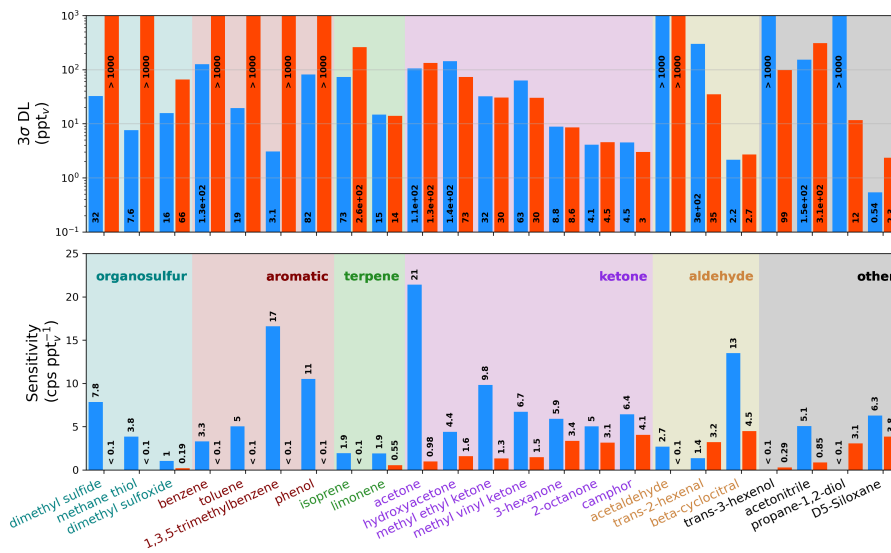


Figure 2. Sensitivities (bottom) and detection limits (top, log y-axis) for the Vocus-CI-ToFMS with NH_4^+ ionization (orange) and H_3O^+ ionization (blue) for 23 analytes from standardized gas cylinders, grouped by functional group/compound type. Sensitivities and detection limits (DLs) are calculated for the molecular ion only (i.e., $\text{A} \cdot \text{NH}_4^+$ for NH_4^+ , or $\text{A} \cdot \text{H}^+$ for H_3O^+), and mass spectral fragments are not included. DL are calculated as 3σ over a 600 second background at 1 Hz.

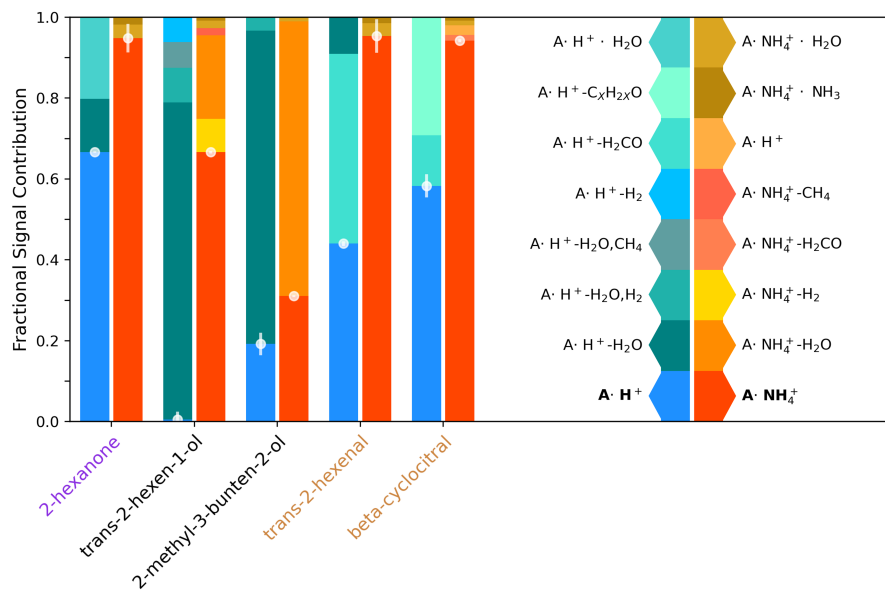


Figure 3. Molecular ion fraction and the contribution of various non-molecular ions for 5 analytes using H₃O⁺ ionization (blue/left) and NH₄⁺ ionization (orange/right). The contribution of the molecular ion is highlighted with a scatter plot and uncertainty bars are standard deviation across 30 mass spectra at 2 Hz. [Data represented in this figure is shown in Table S6.](#)

3.2 Sensitivities, detection limits, and fragmentation

Direct calibrations demonstrate the selectivity of NH_4^+ relative to H_3O^+ ionization for a range of carbonyls, hydrocarbons, alcohols, and organic sulfur compounds (Fig. 2). We observe that H_3O^+ is capable of detecting nearly every compound in this set of analytes from standardized gas cylinders at the molecular ion, which demonstrates the utility of H_3O^+ as a general reagent-ion that allows for detection of reduced and some oxidized species. In contrast, NH_4^+ ionization is more selective toward oxygenates, including saturated and unsaturated ketones, unsaturated aldehydes, and the multi-functional propane-1,2-diol. NH_4^+ 's selectivity toward oxygenates demonstrates its utility for expanding the range of compounds detectable with a single instrument, and supporting identification of molecular ions and fragments detected simultaneously with H_3O^+ . In addition, NH_4^+ does not detect aromatics, small alkenes, and reduced sulfur compounds that H_3O^+ detects well, demonstrating the complimentary nature of these reagent-ions. While Fig. 2 suggests that H_3O^+ detects dimethyl sulfoxide (DMSO), an oxidation product of dimethyl sulfide (Barnes et al., 2006), with a detection limit (DL) of 16 ppt_v, this DL is optimistic because DMSO peak separation is hindered by isobaric ions of protonated benzene and a protonated water cluster of acetic acid. We therefore expect that DMSO cannot be detected with H_3O^+ in the Vocus-CI-ToFMS at concentrations relevant to the marine boundary layer (i.e., <100 ppt_v, Putaud et al. (1999); Sciare et al. (2000); Legrand et al. (2001); Nowak et al. (2001)).

For the compounds detected with both ionization modes, sensitivities and detection limits for H_3O^+ and NH_4^+ are **broadly comparable in the same order of magnitude** (Fig. 2 & A3). NH_4^+ detects the subset of ketones and the unsaturated aldehydes shown in Fig. 2 with a lower or similar DL to H_3O^+ . Propane-1,2-diol, trans-3-hexenol, and D5-siloxane suggest that NH_4^+ has a greater ability than H_3O^+ to detect oxygenated and functionalized compounds, but this is not broadly apparent across the families of compounds we calibrated directly (Fig. 2). This likely arises because the analytes shown in Fig. 2 are limited to compounds amendable to gas cylinder calibration, and are therefore biased toward VOCs and S/IVOCs with minimal oxygenation and relatively high volatility (i.e., $C^* > 9 \times 10^4 \mu\text{g m}^{-3}$; Table S2S4). Despite the compromises in the FIMR temperature made to allow for the switching system (Sect. 3.1) the sensitivities for NH_4^+ ionization reported here are similar to the sensitivities reported in recent NH_4^+ literature (Khare et al., 2022; Xu et al., 2022) (Table S3S5).

Compared to H_3O^+ ionization, NH_4^+ ionization reduces molecular ion fragmentation for functionalized compounds (Fig. 3). We use a molecular ion fraction (Fig. 3; ratio of the molecular ion signal to the total signal from the molecular ion, fragments, and clusters) to analyze the contributions of molecular ions and mass spectral fragments from both NH_4^+ and H_3O^+ ionization for a series of analytes complimentary to those calibrated with standardized gas cylinders (Fig. 2). Alcohols fragment substantially using both reagent-ions; with H_3O^+ , trans-2-hexenol fragments almost completely away from the molecular ion resulting in a near zero molecular ion fraction. This is consistent with the negligible sensitivity to the similarly structured trans-3-hexenol molecular ion (Fig. 2) with H_3O^+ owing to fragmentation (e.g., Pagonis et al., 2019). In contrast, NH_4^+ ionization detects trans-2-hexenol with a molecular ion fraction of 0.67. For the tertiary alcohol, 2-methyl-3-buten-2-ol, (2,3,2-MBO), we observe substantial fragmentation with both ionization modes, but a higher molecular ion fraction under NH_4^+ (i.e., 0.31 with NH_4^+ and 0.19 with H_3O^+). The ketone and aldehydes sampled only fragmented substantially under H_3O^+ ionization, while NH_4^+ retains the molecular structure leading to high molecular ion fraction. This is consistent with the lower NH_4^+

detection limit for the majority of ketones we examined (with the ~~exception of~~ exceptions of acetone and 2-octanone) and the aldehyde trans-2-hexenal (Fig. 2). Our observations suggest that reduced fragmentation has a larger impact on ~~sensitivity~~ between-detection capability of the two reagent-ions for more highly oxidized compounds with multiple functional groups. This is observed for propane-1,2-diol which is readily detected with NH_4^+ but not with H_3O^+ ; ~~the detection of oxidized~~ ROC is discussed further in Sect. 3.5. Overall, these observations demonstrate the high selectivity of NH_4^+ ionization for oxygenates and the benefits of reduced fragmentation with NH_4^+ . Coupling the detection of reduced ROC and organic sulfur from H_3O^+ with the detection of oxygenates from NH_4^+ expands the fraction of atmospheric ROC that we can detect with a single instrument.

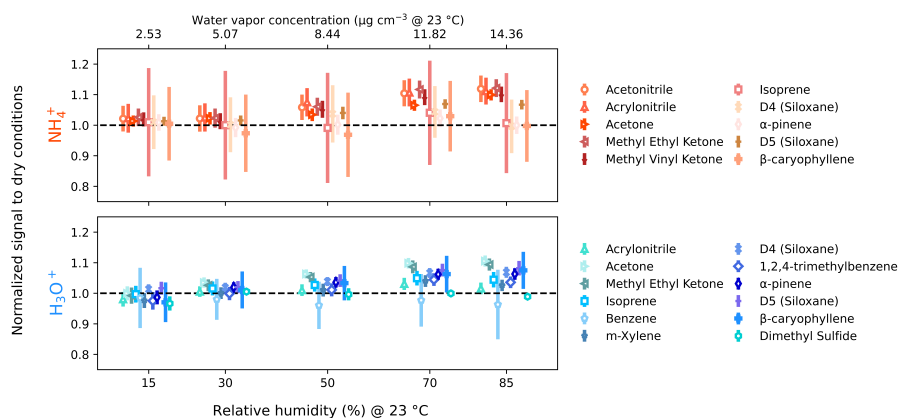


Figure 4. Signal dependence on sample relative humidity for NH_4^+ (top, orange), and H_3O^+ (bottom, blue). Measurements were made at relative humidities of 15, 30, 50, 70, and 85 %; points are offset from these values for visibility. Ethanol, benzene, m-xylene, and 1,2,4-trimethylbenzene are excluded for NH_4^+ due to low signal. Acetonitrile and ethanol are omitted for H_3O^+ due to low transmission through the BSQ. Methyl ethyl ketone is omitted for H_3O^+ due to interference of the reagent-ion cluster $(\text{H}_2\text{O})_3 \cdot \text{H}^+$. The error bars represent propagated relative deviations in dry and humidified signals.

3.3 Impact of sample relative humidity

320 Previous studies have characterized the significant humidity dependence of sensitivity in various CIMS instruments to understand and correct for changing ambient humidity (e.g., Warneke et al., 2001; Gouw and Warneke, 2007; Kari et al., 2018; Zaytsev et al., 2019a). Humidity-driven changes in reagent-ion chemistry, and therefore sensitivity, are generally small in the Vocus-CI-ToFMS due to the large flow of water vapor (i.e., $20 \text{ cm}^3 \text{ min}^{-1}$ (STP)) injected into the ion source (Krechmer et al., 2018; Khare et al., 2022). Varying sample humidity with constant analyte concentration demonstrates ~~humidity-independence~~

325 low humidity dependence with both NH_4^+ and H_3O^+ ionization across a range of reduced and oxygenated ROC (Fig. 4). ~~Humidity-independence~~ We note an approximately 10 % increase in the NH_4^+ sensitivity to nitriles and oxygenates while alkene sensitivities remain unchanged up to 85 % RH. We also observe a slight (5-10%) increase in sensitivity with humidity for oxygenated species with H_3O^+ , while alkene sensitivities are less affected. The low humidity dependence of the Vocus-CI-ToFMS has been demonstrated previously for H_3O^+ for a variety of analytes (Krechmer et al., 2018; Kilgour et al., 2022;

330 Li et al., 2024) and for a select number of small oxygenates, alkenes, and acetonitrile with NH_4^+ (Khare et al., 2022; Xu et al., 2022). We demonstrate ~~humidity-independent sensitivity~~ the low dependence of sensitivity on sample humidity with NH_4^+ ionization under different instrumental conditions and for a selection of analytes including oxygenated alkenes and siloxanes (Fig. 4).

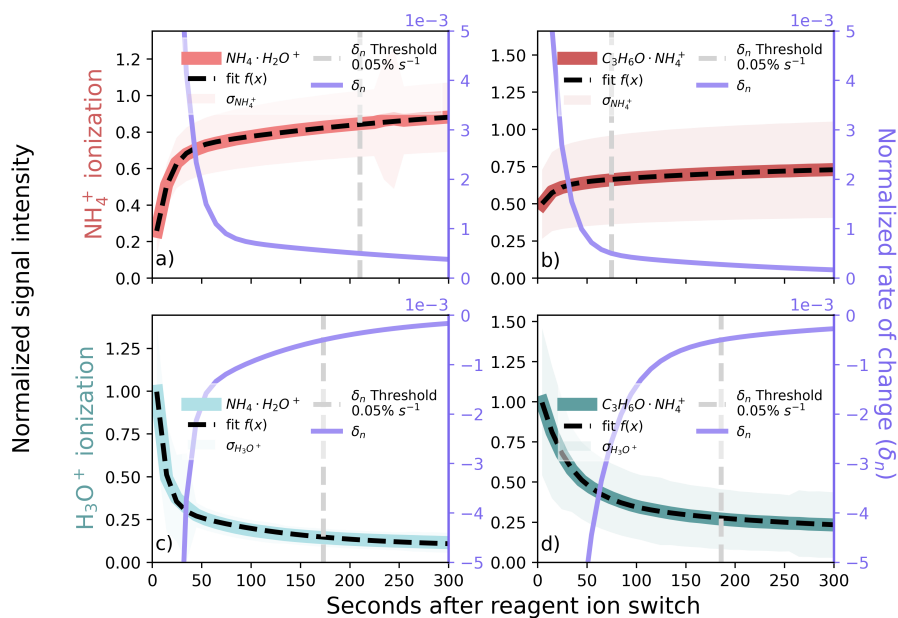


Figure 5. Ion signal after a reagent-ion switch for NH_4^+ (a & b) and H_3O^+ (c & d) in the MEFO data, showing $\text{NH}_4 \cdot \text{H}_2\text{O}^+$ ions (a & c) and $\text{C}_3\text{H}_6\text{O} \cdot \text{NH}_4^+$ (b & d). We grouped ion signals by the time after a switch and normalized the mean of each group by the maximum, and normalized means were fit with a bi-exponential function. The derivative of the fit (δ_n) is displayed on the right axes for (a-d purple traces) and is used as a metric to filter reagent-ion hysteresis. (e) The number of seconds the amount of data removed after a switch as a function of δ_n the selected threshold for various these ions is shown in Fig. S4.

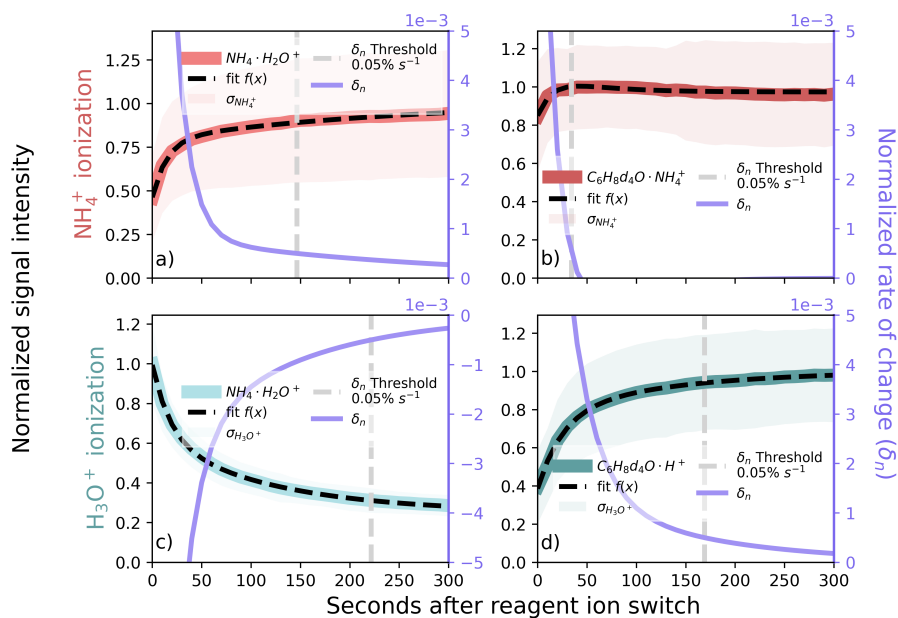


Figure 6. Ion signal after a reagent-ion switch for NH_4^+ (a & b) and H_3O^+ (c & d) in the ARTofMELT data, showing $\text{NH}_4 \cdot \text{H}_2\text{O}^+$ ions (a & c), $\text{C}_6\text{H}_8\text{d}_4\text{O} \cdot \text{NH}_4^+$ (b) and $\text{C}_6\text{H}_8\text{d}_4\text{O} \cdot \text{H}^+$ (d) internal standard ions. We grouped ion signals by the time after a switch and normalized the mean of each group by the maximum, and normalized means were fit with a bi-exponential function. The derivative of the fit (δ_n) is displayed on the right axes (purple traces) and is used as a metric to filter reagent-ion hysteresis. A summary of the amount of data removed as a function of the selected threshold for these ions is shown in Fig. S5.

3.4 Removal of reagent-ion hysteresis from switching

335 ~~reagent-ion~~Reagent-ion chemistry does not stabilize immediately upon switching between NH_4^+ and H_3O^+ ionization. This reagent-ion switch requires adjustment of instrument conditions that impact ion chemistry; these include the reagents introduced into the ion source, the fIMR pressure and voltage gradient, and downstream ion optic voltages ([Table S1](#)). However, instrument conditions for each reagent-ion (Sect. 3.1) are such that analyte detection through the alternate ionization pathway is possible with both NH_4^+ and H_3O^+ ionization (e.g., Zaytsev et al., 2019a). This is in contrast to some other reagent-ion
340 pairs (e.g., CH_3O_2^- and I^-) where instrument conditions differ drastically, and so hysteresis is not observed (e.g., Brophy and Farmer, 2015). As a result, when NH_4^+ and H_3O^+ are paired in a single instrument we observe a distinct transitional period of reagent-ion hysteresis following each reagent-ion switch. The hysteretic period arises from: (1) changes in ion transmission due to instrument conditions, such as ion optics and fIMR settings, which are fast (ones to tens of seconds), and (2) changes in the reagent-ion speciation due to the presence ~~for~~ absence of $\text{NH}_3(\text{g})$, which is slower (tens of seconds to minutes). Periods
345 of hysteresis must be characterized and removed to ensure stable and consistent measurements without drifting sensitivities over the course of each 15-minute measurement period. We accomplish this by monitoring ion stability over a large number of repeated switches.

We compare the ~~use of a reagent-ion signal and an -analyte molecular ion signal~~utility of three ion-types as markers to quantify the timescale of reagent-ion switching hysteresis([Fig. 5](#)): NH_4^+ reagent-ion signal, a persistent ambient NH_4^+ -adduct ion; and known and persistent NH_4^+ -adduct or proton-transfer molecular ions from an internal standard infused in the sampling inlet. We selected ions primarily measured with NH_4^+ ionization because the influence of $\text{NH}_3(\text{g})$ is observed under both H_3O^+ and NH_4^+ ionization modes, whereas the influence of $\text{H}_2\text{O}(\text{g})$ reagent-ions are not observed in NH_4^+ mode ~~-([Fig. S3](#))~~. This arises because $\text{NH}_3(\text{g})$ has a higher proton affinity than $\text{H}_2\text{O}(\text{g})$ (Hunter and Lias, 1998) which causes any $\text{NH}_3(\text{g})$ present in the ion source and fIMR to readily form NH_4^+ or $\text{NH}_4 \cdot \text{H}_2\text{O}^+$ at the expense of H_3O^+ formation.

355 3.4.1 Filtering hysteresis with reagent and persistent ambient ions

~~We follow $\text{NH}_3(\text{g})$ presence and stability by monitoring~~In the absence of a known and persistent signal from an internal standard to diagnose reagent-ion hysteresis, we compare the use of $\text{NH}_4 \cdot \text{H}_2\text{O}^+$ (i.e., the prominent ammonium reagent-ion signal) and $\text{C}_3\text{H}_6\text{O} \cdot \text{NH}_4^+$ (i.e., a ubiquitous analyte-ammonium molecular ion) under both ionization methods. Both $\text{NH}_4 \cdot \text{H}_2\text{O}^+$ and $\text{C}_3\text{H}_6\text{O} \cdot \text{NH}_4^+$ decay after switching to H_3O^+ ionization (Fig. 5a, ~~bc~~, d; $\text{NH}_3(\text{g})$ depletion in the fIMR) and
360 intensify after switching to NH_4^+ ionization (Fig. 5e, ~~da~~, b; $\text{NH}_3(\text{g})$ accumulation in the fIMR).

~~To compare the utility of $\text{NH}_4 \cdot \text{H}_2\text{O}^+$ and $\text{C}_3\text{H}_6\text{O} \cdot \text{NH}_4^+$ signals for filtering reagent-ion hysteresis, we~~We grouped a total of 558 hours of ambient $\text{NH}_4^+/\text{H}_3\text{O}^+$ 15-minute reagent-ion switching observations from MEFO (Sect. 2.5) by time after a reagent-ion switch. We normalized the mean signal (in 10 second intervals starting at 5 seconds into a switch) to the maximum and fit the normalized data with a bi-exponential function (Fig. 5). The bi-exponential function describes changes
365 in both instrument conditions (fast) and equilibration of $\text{NH}_3(\text{g})$ in the ion source and fIMR that drives reagent-ion chemical speciation (slow). We use the derivative of this decay function (δ_n) to quantify a normalized rate of change in the ion signal as

a function of the time after a switch (Purple lines in Fig. 5a-d). We use δ_n to set a threshold for filtering hysteresis, removing data before δ_n reaches the set threshold. For all ions in Fig. 5, δ_n changes rapidly in the first ~ 100 s after a reagent-ion switch and slowly approaches but does not reach zero on the measurement timescale (900 s) (Fig. S4), likely due to the time scale for complete NH_3 (g) equilibration with instrument surfaces.

Monitoring $\text{NH}_4 \cdot \text{H}_2\text{O}^+$ δ_n has the benefit of being directly related to the abundance of reagent-ion; however, both the decay of $\text{NH}_4 \cdot \text{H}_2\text{O}^+$ in H_3O^+ ionization mode and its initial increase in NH_4^+ ionization mode is driven largely by changes in the BSQ mass range. We are able to avoid the impacts of changing BSQ mass range by monitoring an ion with higher m/z . Additionally, using an analyte for filtering reagent-ion hysteresis means that we are using a direct measurement of the formation of analyte ions for NH_4^+ ionization and a direct measurement of contamination from other reagent-ion chemistry with H_3O^+ ionization. ~~For these reasons we decided to~~ Therefore, in the absence of an internal standard (Sect. 3.4.2), we use the persistent ambient ion $\text{C}_3\text{H}_6\text{O} \cdot \text{NH}_4^+$ to monitor hysteresis. We acknowledge this choice brings the complication of varying ambient concentrations in time; however, due to the substantial averaging over a multi-week measurement period, normalized mean time variation over the 15-minute (900 s) acquisition time should be mainly due to changes in reagent-ion chemistry. Despite this, future iterations of this approach would benefit from This approach brings two major complications: (1) variable contributions of isomers with potentially disparate sensitivities (e.g., acetone and propionaldehyde), and (2) potentially variable ambient concentrations. A switch-by-switch analysis of hysteresis from MEFO (available as Fig. S6) shows that the $0.05\% \text{ s}^{-1}$ δ_n cutoffs for $\text{C}_3\text{H}_6\text{O} \cdot \text{NH}_4^+$ calculated in Fig. 5b, d do not capture the majority of the switch-by-switch cutoffs (37% for NH_4^+ and 39% for H_3O^+). Therefore, if a persistent ambient ion is used to diagnose hysteresis timescales, this should be done on a switch-by-switch basis. This variability may be associated with ambient variations in the $\text{C}_3\text{H}_6\text{O} \cdot \text{NH}_4^+$ signal which can be avoided by applying our method on the described in Fig. 5 to a persistent and known signal from an internal standard infused into the sampling inlet. (Sect. 3.4.2).

The choice of δ_n threshold represents a compromise between ion chemistry stability and data loss. For both reagent and analyte ions, the amount of data removed becomes very sensitive to a small decrease in the δ_n threshold below $\sim 0.05\% \text{ s}^{-1}$ (Fig. 5e)-A S4). During the deployment in MEFO, a $0.05\% \text{ s}^{-1}$ threshold applied to $\text{C}_3\text{H}_6\text{O} \cdot \text{NH}_4^+$ results in the loss of ~ 185 s (Fig. 5d) and ~ 75 s (Fig. 5b) of data per switch with H_3O^+ and NH_4^+ ionization, respectively. For Optimizing ion chemistry stability, while preserving data coverage results in the loss of ~ 260 s (75 s for NH_4^+ and 185 s for H_3O^+) of data on a reagent switching full cycle (1800 s), corresponding to $\sim 86\%$ data retention for 15-minute reagent-ion switching intervals.

3.4.2 Filtering hysteresis with reagent and internal standard ions

When an internal standard signal is available, as in the ARTofMELT expedition (Sect. 2.5.1), this corresponds to 2.6), reagent-ion hysteresis can be more reliably monitored using known unique and persistent molecular ions. We applied the δ_n thresholding method to a 2-week period from the ARTofMELT data set (from May 17th to May 31st of 2023). We quantify the timescale of reagent-ion hysteresis by monitoring the internal standard signal of 2-hexanone- d_4 as $\text{C}_6\text{H}_8\text{d}_4\text{O} \cdot \text{NH}_4^+$ with NH_4^+ ionization (Fig. 6b) and as $\text{C}_6\text{H}_8\text{d}_4\text{O} \cdot \text{H}^+$ with H_3O^+ ionization (Fig. 6d). For direct comparison to Sect. 3.4.1, we also use the

reagent ion $\text{NH}_4 \cdot \text{H}_2\text{O}^+$ under both NH_4^+ (Fig. 6a) and H_3O^+ (Fig. 6c). Notably, in this marine environment the ambient $\text{C}_3\text{H}_6\text{O} \cdot \text{NH}_4^+$ signal is highly variable, precluding its use for filtering reagent-ion hysteresis (Fig. S7), further motivating the use of an internal standard to diagnose reagent-ion hysteresis. A $0.05\% \text{ s}^{-1}$ threshold applied to 2-hexanone- d_4 results in the loss of 34 seconds from NH_4^+ ionization after a switch (Fig. 6b) and 168 seconds from H_3O^+ ionization (Fig. 6d). This results in ~~~14% of all 19% of H_3O^+ data being removed. This result is qualitatively similar to that suggested by Zaytsev et al. (2019a) for NH_4^+ and H_3O^+ switching in an Ionicon PTR3: ~120 s and 4% of NH_4^+ ionization from 15-minute switching, or ~60 s of data removed after switching to H_3O^+ 89% total data retention over a full (1800 s) switching cycle. It's worth noting that under both ionization modes, the hysteresis timescale for the $\text{NH}_4 \cdot \text{H}_2\text{O}^+$ is longer (Fig. 6a & c, S8) than the 2-hexanone- d_4 internal standard ion. This suggests that a conservative approach to monitoring ion chemistry could be to use the reagent-ions for establishing hysteresis timescales. However, the impacts of the BSQ on reagent-ions raises concerns of how representative the reagent-ion signal is of true composition in the fIMR (Krechmer et al., 2018; Khare et al., 2022; Xu et al., 2022). A switch-by-switch analysis of variation in the hysteresis timescale (available as Fig. S8) demonstrates that the cutoffs calculated in Fig. 6 for 2-hexanone- d_4 capture the majority of variability in hysteresis timescale for independent switches (75% for NH_4^+ and 72% for H_3O^+). Our results using an internal standard for reagent-ion hysteresis filtering are qualitatively similar to the analysis above (Sect. 3.4.1) using a persistent ambient ion, though there is less data removed from NH_4^+ ionization, respectively. The. Rather than resulting from use of an ambient or internal standard ion, this difference in hysteresis time is likely the result of having more similar BSQ settings between the two ionization modes during the ARTofMELT campaign (Table S1). The smaller change in BSQ settings results in a faster change in instrument conditions impacting ion transmission. The approach we describe here can be applied easily to other instruments and at different instrument conditions (e.g., fIMR temperature and pressure) to best balance the need for both measurement stability and data coverage. While the use of an internal standard signal is ideal for diagnosing reagent-ion switching hysteresis, the choice of both product molecular ions and rate-of-change threshold must be optimized for each application and sampling environment. Overall, our results are qualitatively similar to hysteresis timescales suggested by Zaytsev et al. (2019a) for NH_4^+ and H_3O^+ switching in an Ionicon PTR3: ~120 s and ~60 s of data removed after switching to H_3O^+ and NH_4^+ ionization, respectively.~~

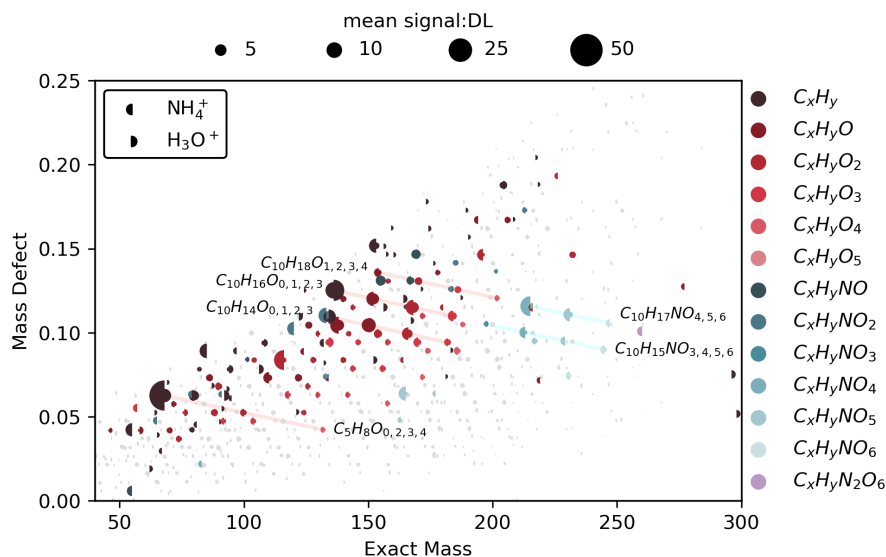


Figure 7. Campaign mean mass defect plots for NH_4^+ and H_3O^+ ionization from deployment in MEFO. The NH_4^+ mass spectrum is displayed as a left half-circle and the H_3O^+ is displayed as a right half-circle. Points are sized by the average signal across the campaign divided by the detection limit signal (DL: 3σ of campaign zero air background). The reagent-ion masses have been removed from the ion molecular mass. The top 100 ions in terms of signal-to-DL ratio for both reagent-ions have been colored according to their molecular formulae with periods of reagent-ion hysteresis removed (Sect. 3.4). [A total of 725 ions are shown, and selected ions and their signal-to-DL ratios are displayed in a bar chart format in Fig. S9.](#)

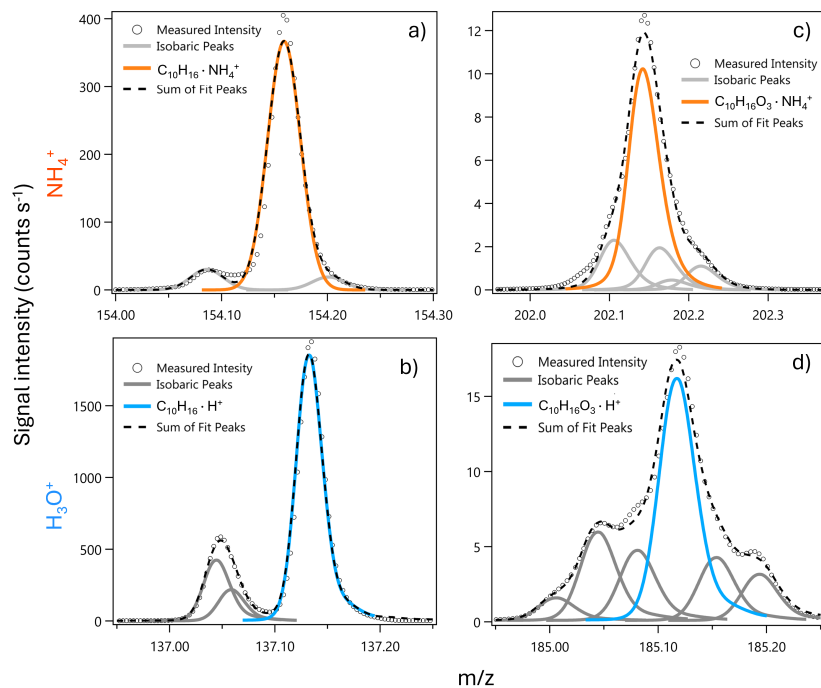


Figure 8. Selected campaign average high resolution mass spectra [from MEFO](#) for (a & b) monoterpane ($C_{10}H_{16}$) and (c & d) monoterpane oxygenate ($C_{10}H_{16}O_3$) molecular ions detected with NH_4^+ (a & c, orange) and H_3O^+ (b & d, blue).

We compare the capabilities of NH_4^+ and H_3O^+ reagent-ions in a single instrument using ambient observations from MEFO (Sect. 2.5.1-2.5). Switching between H_3O^+ and NH_4^+ on a 15-minute timescale over the 21-day deployment allows us to directly compare the two reagent-ions in a predominantly biogenic environment (Hunter et al., 2017; Vermeuel et al., 2023a; Riches et al., 2024; Link et al., 2024). A single instrument approach avoids inlet and instrument design influences on detection that would otherwise complicate a direct reagent-ion comparison (e.g., Riva et al., 2019). Previously Zaytsev et al. (2019a) used a switching $\text{NH}_4^+/\text{H}_3\text{O}^+$ Ionicon PTR3 with a modified helical tripole reaction chamber to measure products from the $\cdot\text{OH}$ initiated oxidation of 3-methylcatechol. This chamber study demonstrated the sets of compounds detected by each reagent-ion and concluded that NH_4^+ is able to detect larger, more functionalized molecules, while H_3O^+ is able to detect smaller organic molecules (Zaytsev et al., 2019a). To facilitate a direct and quantitative reagent-ion comparison, we use the ratio of campaign average ambient signal to detection limit signal (i.e., 3σ of the background) for each ion as a measure of the signal-to-noise ratio (Fig. 7). With the assumption that ambient concentrations measured with each reagent-ion over the campaign mean are equivalent, a higher signal-to-DL ratio also implies a lower detection limit. This analysis allows us to evaluate the relative capability of each reagent-ion without direct calibrations for multifunctional biogenic organic compounds (e.g., Hunter et al., 2017; Vermeuel et al., 2023a; Link et al., 2024).

NH_4^+ ionization detects oxygen-containing species with a higher signal-to-noise ratio than H_3O^+ . At MEFO, four series of $\text{C}_x\text{H}_y\text{O}_z$ ions dominate our mass spectrum (highlighted in Fig. 7): $\text{C}_{10}\text{H}_{16}\text{O}_n$, $\text{C}_{10}\text{H}_{14}\text{O}_n$, $\text{C}_{10}\text{H}_{18}\text{O}_n$, and $\text{C}_5\text{H}_8\text{O}_n$ which represent a mixture of biogenic terpenoid compounds and their early generation oxidation products. The $\text{C}_{10}\text{H}_{16}\text{O}_n$ and $\text{C}_{10}\text{H}_{14}\text{O}_n$ series suggest a mixture of primary emissions, such as citral ($\text{C}_{10}\text{H}_{16}\text{O}$; $C^* = 1 \times 10^6 \mu\text{g m}^{-3}$) and thymol or carvone ($\text{C}_{10}\text{H}_{14}\text{O}$; $C^* = 1 - 9 \times 10^5 \mu\text{g m}^{-3}$) (McKinney et al., 2011; Kaser et al., 2013; Vermeuel et al., 2023a), and oxidation products of other terpenoids. H_3O^+ detects the reduced $\text{C}_{10}\text{H}_{14}$ species with higher signal-to-noise compared to NH_4^+ , with signal-to-DL ratios of 10.5 and 6.00, respectively. Similarly, H_3O^+ detects $\text{C}_{10}\text{H}_{16}$ with a signal-to-DL ratio of 23.5, compared to 14.3 for NH_4^+ . Following this $\text{C}_{10}\text{H}_{16}\text{O}_n$ series, the $n = 1$ ion is detected with a signal-to-DL ratio of 6.31 with H_3O^+ and 10.8 with NH_4^+ . The tendency toward increased signal-to-noise with oxygenation for NH_4^+ ionization continues in the $\text{C}_{10}\text{H}_{14,16}\text{O}_n$ series up to $\text{C}_{10}\text{H}_{14,16}\text{O}_3$ (with C^* between 4×10^2 and $9 \times 10^3 \mu\text{g m}^{-3}$, Table S4S7). The $\text{C}_{10}\text{H}_{18}\text{O}_n$ series lacks a $\text{C}_{10}\text{H}_{18}$ ion and the distribution in the x-y scatter between the $\text{C}_{10}\text{H}_{16}$ and $\text{C}_{10}\text{H}_{18}\text{O}$ peaks is bimodal (Fig. S3S10), which suggests multiple paths to form $\text{C}_{10}\text{H}_{18}\text{O}$ ions. These paths are likely (1) primary emissions of $\text{C}_{10}\text{H}_{18}\text{O}$ terpenoid compounds with similar emission profiles to monoterpenes and (2) water clusters formed with monoterpenes ($\text{C}_{10}\text{H}_{18} \cdot \text{H}_2\text{O} \cdot \text{H}^+$ and $\text{C}_{10}\text{H}_{18} \cdot \text{H}_2\text{O} \cdot \text{NH}_4^+$). The $\text{C}_5\text{H}_8\text{O}_n$ series represents a combination of fragments, primary emissions and oxidation products. The C_5H_8 ion is likely a mixture of isoprene and fragments from larger oxygenates and 2,3,2-MBO with both reagent-ions (e.g., Kilgour et al., 2024). Within the $\text{C}_5\text{H}_8\text{O}_n$ series, the C_5H_8 signal-to-DL ratio is larger than expected with NH_4^+ ionization; we suspect that this is due partly to fragmentation of other compounds into the C_5H_8 mass. The NH_4^+ sensitivity to isoprene is very low; however 2,3,2-MBO fragments substantially into C_5H_8 through dehydration of the tertiary alcohol group (Fig. 3). Fragmentation into C_5H_8 combined with a low background (Fig. A3 & S4S11)

leads to a very large signal-to-DL ratio (Fig. 7). The $C_5H_8O_3$ and $C_5H_8O_4$ peaks are likely oxidation products of isoprene and
460 2,3,2-MBO, while $C_5H_8O_2$ is likely an isoprene oxidation product (Saunders et al., 2003; Jenkin et al., 2015).

NH_4^+ can detect organic nitrates that easily fragment with H_3O^+ (Aoki et al., 2007; Duncianu et al., 2017) and so often go un-
detected in ambient measurements with H_3O^+ ionization (Fig. 7). Organic nitrates ionized with H_3O^+ fragment to form nitric
acid (HNO_3) or nitronium ions (NO_2^+), where the loss of HNO_3 results in fragmentation into the masses for other oxygenates
(Aoki et al., 2007). The two predominant series of organic nitrate ions ($C_{10}H_{15}NO_n$ and $C_{10}H_{17}NO_n$ with C^* down to ~~10s~~ tens
465 of $\mu g\ m^{-3}$; Table S4S7) are generally detected with a higher signal-to-DL ratio with NH_4^+ ionization compared to H_3O^+ ion-
ization, if the ion is detected with H_3O^+ at all (Fig. 7). The exception is $C_{10}H_{15}NO_3$ which is detected at higher signal-to-DL
(2.13) with H_3O^+ ionization compared to NH_4^+ (0.774); though this ion may arise from dehydration of hydroxy nitrates (i.e.,
 $C_{10}H_{17}NO_4-H_2O$) and that H_3O^+ is fragmenting larger organic nitrates into the $C_{10}H_{15}NO_3$ ion. The nitrates we observe are
potentially a mixture of carbonyl, hydroxy, and peroxy nitrates derived from the oxidation of monoterpenes ($C_{10}H_{16}$) and po-
470 tentially other terpenoid ($C_{10}H_{16}O/C_{10}H_{14}O$) precursors (Table S5, Fry et al., 2013; Jenkin et al., 2015; Faxon et al., 2018; Bates et al., 2022).
(Table S8, Fry et al., 2013; Jenkin et al., 2015; Faxon et al., 2018; Bates et al., 2022). Additionally, $C_5H_{11}NO_5$ and $C_5H_9NO_5$
are detected using both reagent-ions but both with higher signal-to-DL ratio with NH_4^+ . $C_5H_{11}NO_5$ is likely a nitrate from the
oxidation 2,3,2-MBO while both 2,3,2-MBO and isoprene could form the $C_5H_9NO_5$ ion (Link et al., 2024).

NH_4^+ ionization's ability to detect oxygenated compounds with higher signal-to-noise ratio and lower detection limits than
475 H_3O^+ arises from two main factors. First, NH_4^+ is a softer ionization method compared to H_3O^+ , resulting in less molecular
ion fragmentation (Sect. 3.2). This is evident in our ambient data for the known H_3O^+ monoterpene fragment, $C_6H_8 \cdot H^+$
compared to the analogous fragment with NH_4^+ ionization, $C_6H_8 \cdot NH_4^+$. The fragment is present in NH_4^+ ionization mode at
a 1:10 fragment-to-molecular-ion ratio, compared to a 1:1 ratio with H_3O^+ under our fIMR conditions (Fig. S3S10). Second,
 NH_4^+ has higher selectivity toward oxygenates compared to H_3O^+ (Sect. 3.2). Our ambient reagent-ion switching observations
480 further demonstrate this selectivity (Fig. 8 & A3). The monoterpenes ($C_{10}H_{16}$) are easily distinguished from isobaric ions with
both H_3O^+ and NH_4^+ , but oxygenates ($C_{10}H_{16}O_3$) have multiple isobaric interferences with H_3O^+ (Fig. 8). Both higher
selectivity and reduced fragmentation contribute to fewer isobaric ions with NH_4^+ . While our observations demonstrate the
utility of NH_4^+ for detecting oxidized species that H_3O^+ ionization struggles to detect (e.g., Yuan et al., 2017; Riva et al.,
2019; Pagonis et al., 2019; Coggon et al., 2024), the extent of fragmentation for specific compounds is difficult to diagnose in
485 ambient, and complex laboratory, mass spectra. Overall, our ambient reagent-ion comparison demonstrates quantitatively that
 NH_4^+ is complementary to H_3O^+ , and together these two reagent-ions allow improved detection and identification of a range
of biogenic reactive organic carbon compounds and their early generation oxidation products.

4 Conclusions

To expand the range of ROC detectable with a single chemical ionization instrument, we present an approach to combine
490 two positive reagent-ions, NH_4^+ and H_3O^+ , in a Vocus-CI-ToFMS. To accommodate the need for a constant ion-molecule
reactor temperature during switching, we apply an E/N space scanning approach to select fIMR conditions compatible with

both reagent-ions. We characterize the ability of NH_4^+ and H_3O^+ to detect a range of reduced and oxygenated VOCs and S/IVOCs through analysis of laboratory standards and find that H_3O^+ detects reduced species well and fragments functionalized oxygenates away from the molecular ion, while NH_4^+ retains the molecular ion and allows for improved detection of oxygenates. We find that fragmentation generally correlated with E/N , while sensitivity is impacted by a combination of ion transmission, competing ionization pathways, and molecular ion fragmentation. ~~Switching between reagent-ions results in a period of hysteresis which we characterize and filter using a ubiquitous analyte ion~~ To diagnose and quantify the timescales for reagent-ion switching hysteresis we compare the use of three ion-types: NH_4^+ reagent ions; a persistent ambient NH_4^+ -adduct ion; and NH_4^+ -adduct or proton-transfer molecular ions from an internal standard infused in the sampling inlet. Reagent-ion signal variability at each switch is driven largely by changes in ion transmission so is less representative of ion chemistry, ~~Optimizing ion chemistry stability, while preserving data coverage results in the loss of~~ while monitoring a product ion is more directly related to ionization reactions taking place in the FMR. An internal standard signal provides the ideal means to monitor reagent-ion hysteresis with a known and persistent product ion; however, persistent ambient ions and internal standard product ions can produce similar rates of data retention (~~~260 of data on a reagent switching full cycle (1800), corresponding to ~86~~ 86-89 % data retention for 15-minute switching intervals across a full 1800 s switching cycle with a $0.05\% \text{ s}^{-1}$ rate-of-change threshold). We deploy our $\text{NH}_4^+/\text{H}_3\text{O}^+$ reagent-ion switching Vocus-CI-ToFMS during a 3-week period at a rural pine forest (Manitou experimental forest observatory) to facilitate a direct and quantitative ~~comparison of the reagent-ions~~ reagent-ion comparison. Our ambient observations demonstrate that NH_4^+ detects oxygenated ROC with higher signal-to-noise and lower DL, including organic nitrates that H_3O^+ does not detect, while H_3O^+ detects reduced species that are undetectable with NH_4^+ . $\text{NH}_4^+/\text{H}_3\text{O}^+$ reagent-ion switching takes advantage of the complimentary nature of the two reagent-ions to expand the range of ROC detectable with a single instrument.

Appendix A

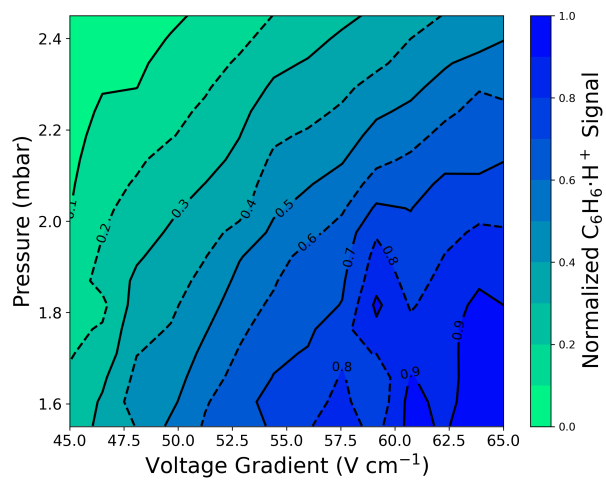


Figure A1. Normalized signal intensity for benzene measured with H_3O^+ ($\text{C}_6\text{H}_6 \cdot \text{H}^+$) from pressure-voltage gradient scans.

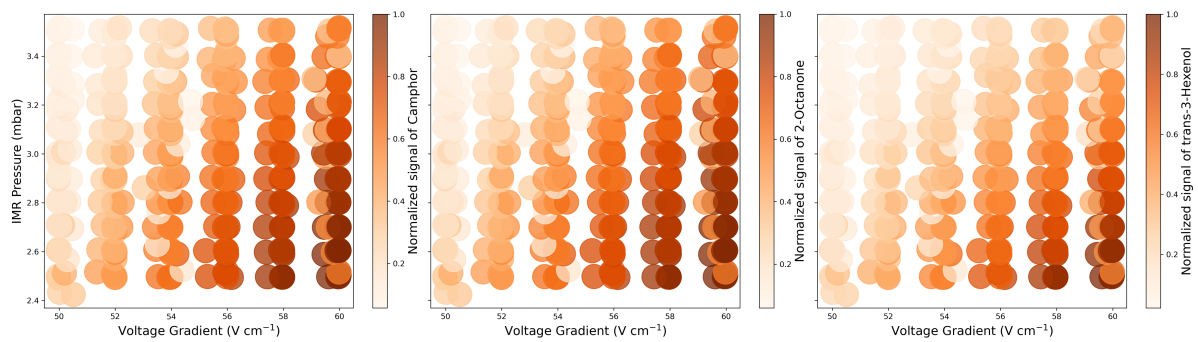


Figure A2. Normalized signal intensity for camphor (left), 2-octanone (middle), and trans-3-hexenol (right) measured with NH_4^+ ($\text{C}_{10}\text{H}_{16}\text{O} \cdot \text{NH}_4^+$, $\text{C}_8\text{H}_{16}\text{O} \cdot \text{NH}_4^+$, and $\text{C}_6\text{H}_{12}\text{O} \cdot \text{NH}_4^+$ respectively).

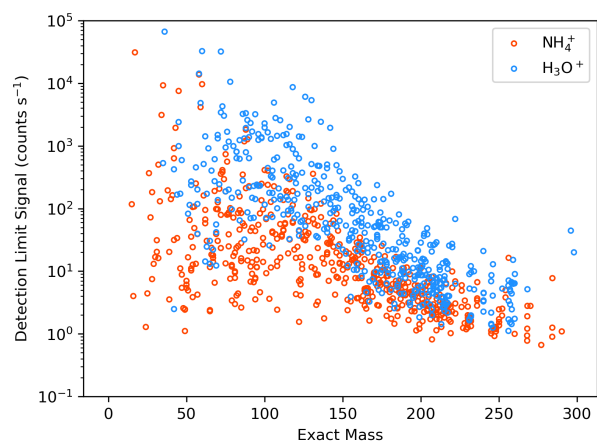


Figure A3. Mass dependent campaign average detection limit signal for ions detected with NH_4^+ (orange) and H_3O^+ (blue). The reagent-ion masses have been removed from ion exact masses.

Author contributions. CLZ & MDW designed research, CLZ collected and analyzed field and laboratory data with significant input from MDW, CLZ & MDW wrote the manuscript.

515 *Code and data availability.* Data and python code required to regenerate figures are available at <https://doi.org/10.7910/DVN/FL0CZM>
(Zang and Willis, 2024).

Competing interests. The authors declare no competing interests.

Acknowledgements. This material is based on work supported in part by the US National Science Foundation under Grant No. AGS-2211153, and by Colorado State University ([CSU](#)). We thank the Flux Closure Study (FluCS) team with researchers from ~~Colorado State University~~
520 ~~(CSU)~~[CSU](#), University of Minnesota-Twin Cities (UM), and Indiana University Bloomington (IU), including Sara Williams (CSU), Mj Riches (CSU), Matson Pothier (CSU), Michael Link (CSU), Lauren Garofalo (CSU), Delphine Farmer (CSU), Michael Vermeuel (UM), Dylan Millet (UM), Emily Reidy (IU), Paige Price (IU), Brandon Bottorff (IU), and Phillip Stevens (IU), for their support with field observations at MEFO. We also acknowledge Tucker Melles (CSU) for supporting field observations at MEFO [and ARTofMELT](#). We thank the National Center for Atmospheric Research (NCAR) for [MEFO](#) field site maintenance, and Paula Fornwalt and Steve Alton from United
525 States Forest Service (USFS) for support during field observations. [This work is part of the ARTofMELT \(Atmospheric rivers and the onset of Arctic melt\) project. The ARTofMELT expedition was supported and organized by the Swedish Polar Research Secretariat \(SPRS\) on the Swedish research icebreaker Oden in spring 2023 under the SWEDARCTIC program. Support also came from the Swedish Council for Research Infrastructures \(Grant 2021-00153\) and the Knut and Alice Wallenberg Foundation \(Grant 2016-0024\). The authors are grateful to the co-Chief Scientists Michael Tjernström and Paul Zieger, the SPRS coordinator Åsa Lindgren and the SPRS support team, and to Captain](#)
530 [Mattias Petersson and the crew on Oden.](#)

References

- Adams, N., Babcock, L., Mostefaoui, T., and Kerns, M.: Selected ion flow tube study of NH_4^+ association and of product switching reactions with a series of organic molecules, *International Journal of Mass Spectrometry*, 223–224, 459–471, 2003.
- 535 Agarwal, B., Gonzalez-Mendez, R., Lanza, M., Sulzer, P., Mark, T. D., Thomas, N., and Mayhew, C. A.: Sensitivity and selectivity of switchable reagent ion soft chemical ionization mass spectrometry for the detection of picric acid, *J Phys Chem A*, 118, 8229–36, <https://doi.org/10.1021/jp5010192>, 2014.
- Aljawhary, D., Lee, A. K. Y., and Abbatt, J. P. D.: High-resolution chemical ionization mass spectrometry (ToF-CIMS): application to study SOA composition and processing, *Atmospheric Measurement Techniques*, 6, 3211–3224, <https://doi.org/10.5194/amt-6-3211-2013>, 2013.
- Aoki, N., Inomata, S., and Tanimoto, H.: Detection of C1–C5 alkyl nitrates by proton transfer reaction time-of-flight mass spectrometry, *International Journal of Mass Spectrometry*, 263, 12–21, <https://doi.org/10.1016/j.ijms.2006.11.018>, 2007.
- 540 Barnes, I., Hjorth, J., and Mihalopoulos, N.: Dimethyl Sulfide and Dimethyl Sulfoxide and Their Oxidation in the Atmosphere, *Chemical Reviews*, 106, 940–975, <https://doi.org/10.1021/cr020529+>, 2006.
- Bates, K. H., Burke, G. J. P., Cope, J. D., and Nguyen, T. B.: Secondary organic aerosol and organic nitrogen yields from the nitrate radical (NO_3) oxidation of alpha-pinene from various RO_2 fates, *Atmospheric Chemistry and Physics*, 22, 1467–1482, <https://doi.org/10.5194/acp-22-1467-2022>, 2022.
- 545 Berndt, T., Scholz, W., Mentler, B., Fischer, L., Hoffmann, E. H., Tilgner, A., Hyttinen, N., Prisle, N. L., Hansel, A., and Herrmann, H.: Fast Peroxy Radical Isomerization and OH Recycling in the Reaction of OH Radicals with Dimethyl Sulfide, *J Phys Chem Lett*, 10, 6478–6483, <https://doi.org/10.1021/acs.jpcclett.9b02567>, 2019.
- Bianchi, F., Kurten, T., Riva, M., Mohr, C., Rissanen, M. P., Roldin, P., Berndt, T., Crouse, J. D., Wennberg, P. O., Mentel, T. F., Wildt, J., 550 Junninen, H., Jokinen, T., Kulmala, M., Worsnop, D. R., Thornton, J. A., Donahue, N., Kjaergaard, H. G., and Ehn, M.: Highly Oxygenated Organic Molecules (HOM) from Gas-Phase Autoxidation Involving Peroxy Radicals: A Key Contributor to Atmospheric Aerosol, *Chem Rev*, 119, 3472–3509, <https://doi.org/10.1021/acs.chemrev.8b00395>, 2019.
- Blomquist, B., Huebert, B. J., Fairall, C. W., and Faloon, I.: Determining the sea-air flux of dimethylsulfide by eddy correlation using mass spectrometry, *Atmos Meas Tech*, 3, 1–20, 2010.
- 555 Brophy, P. and Farmer, D. K.: A switchable reagent ion high resolution time-of-flight chemical ionization mass spectrometer for real-time measurement of gas phase oxidized species: characterization from the 2013 southern oxidant and aerosol study, *Atmospheric Measurement Techniques*, 8, 2945–2959, <https://doi.org/10.5194/amt-8-2945-2015>, 2015.
- Burkart, J., Hodshire, A. L., Mungall, E. L., Pierce, J. R., Collins, D. B., Ladino, L. A., Lee, A. K. Y., Irish, V., Wentzell, J. J. B., Lig- 560 gio, J., Papayriakou, T., Murphy, J., and Abbatt, J.: Organic Condensation and Particle Growth to CCN Sizes in the Summertime Marine Arctic Is Driven by Materials More Semivolatile Than at Continental Sites, *Geophysical Research Letters*, 44, 10,725–10,734, <https://doi.org/10.1002/2017gl075671>, 2017.
- Canaval, E., Hyttinen, N., Schmidbauer, B., Fischer, L., and Hansel, A.: NH_4^+ Association and Proton Transfer Reactions With a Series of Organic Molecules, *Front Chem*, 7, 191, <https://doi.org/10.3389/fchem.2019.00191>, 2019.
- Claffin, M. S., Pagonis, D., Finewax, Z., Handschy, A. V., Day, D. A., Brown, W. L., Jayne, J. T., Worsnop, D. R., Jimenez, J. L., Ziemann, 565 P. J., de Gouw, J., and Lerner, B. M.: An in situ gas chromatograph with automatic detector switching between PTR- and EI-TOF-MS: isomer-resolved measurements of indoor air, *Atmospheric Measurement Techniques*, 14, 133–152, <https://doi.org/10.5194/amt-14-133-2021>, 2021.

- Coggon, M. M., Gkatzelis, G. I., McDonald, B. C., Gilman, J. B., Schwantes, R. H., Abuhassan, N., Aikin, K. C., Arend, M. F., Berkoff, T. A., Brown, S. S., Campos, T. L., Dickerson, R. R., Gronoff, G., Hurley, J. F., Isaacman-VanWertz, G., Koss, A. R., Li, M., McKeen, S. A., Moshary, F., Peischl, J., Pospisilova, V., Ren, X., Wilson, A., Wu, Y., Trainer, M., and Warneke, C.: Volatile chemical product emissions enhance ozone and modulate urban chemistry, *Proc Natl Acad Sci U S A*, 118, <https://doi.org/10.1073/pnas.2026653118>, 2021.
- 570 Coggon, M. M., Stockwell, C. E., Claffin, M. S., Pfannerstill, E. Y., Xu, L., Gilman, J. B., Marcantonio, J., Cao, C., Bates, K., Gkatzelis, G. I., Lamplugh, A., Katz, E. F., Arata, C., Apel, E. C., Hornbrook, R. S., Piel, F., Majluf, F., Blake, D. R., Wisthaler, A., Canagaratna, M., Lerner, B. M., Goldstein, A. H., Mak, J. E., and Warneke, C.: Identifying and correcting interferences to PTR-ToF-MS measurements of isoprene and other urban volatile organic compounds, *Atmospheric Measurement Techniques*, 17, 801–825, <https://doi.org/10.5194/amt-17-801-2024>, 2024.
- Croft, B., Martin, R. V., Leaitch, W. R., Burkart, J., Chang, R. Y. W., Collins, D. B., Hayes, P. L., Hodshire, A. L., Huang, L., Kodros, J. K., Moravek, A., Mungall, E. L., Murphy, J. G., Sharma, S., Tremblay, S., Wentworth, G. R., Willis, M. D., Abbatt, J. P. D., and Pierce, J. R.: Arctic marine secondary organic aerosol contributes significantly to summertime particle size distributions in the Canadian Arctic Archipelago, *Atmospheric Chemistry and Physics*, 19, 2787–2812, <https://doi.org/10.5194/acp-19-2787-2019>, 2019.
- 580 Croft, B., Martin, R. V., Moore, R. H., Ziemba, L. D., Crosbie, E. C., Liu, H., Russell, L. M., Saliba, G., Wisthaler, A., Müller, M., Schiller, A., Galf, M., Chang, R. Y. W., McDuffie, E. E., Bilsback, K. R., and Pierce, J. R.: Factors controlling marine aerosol size distributions and their climate effects over the northwest Atlantic Ocean region, *Atmospheric Chemistry and Physics*, 21, 1889–1916, <https://doi.org/10.5194/acp-21-1889-2021>, 2021.
- 585 Crouse, J. D., McKinney, K. A., Kwan, A. J., and Wennberg, P. O.: Measurement of gas-phase hydroperoxides by chemical ionization mass spectrometry, *Analytical Chemistry*, 78, 6726–6732, <https://doi.org/10.1021/ac0604235>, 2006.
- Crouse, J. D., Nielsen, L. B., Jorgensen, S., Kjaergaard, H. G., and Wennberg, P. O.: Autoxidation of Organic Compounds in the Atmosphere, *Journal of Physical Chemistry Letters*, 4, 3513–3520, <https://doi.org/10.1021/jz4019207>, 2013.
- Deming, B. L., Pagonis, D., Liu, X., Day, D. A., Talukdar, R., Krechmer, J. E., Gouw, J. A. D., Jimenez, J. L., and Ziemann, P. J.: Measurements of delays of gas-phase compounds in a wide variety of tubing materials due to gas-wall interactions, *Atmos. Meas. Tech*, 12, 3453–3461, <https://doi.org/10.5194/amt-12-3453-2019>, 2019.
- Donahue, N. M., Epstein, S. A., Pandis, S. N., and Robinson, A. L.: A two-dimensional volatility basis set: 1. organic-aerosol mixing thermodynamics, *Atmospheric Chemistry and Physics*, 11, 3303–3318, <https://doi.org/10.5194/acp-11-3303-2011>, 2011.
- Duncanianu, M., David, M., Kartigeyane, S., Cirtog, M., Doussin, J.-F., and Picquet-Varrault, B.: Measurement of alkyl and multi-functional organic nitrates by proton-transfer-reaction mass spectrometry, *Atmospheric Measurement Techniques*, 10, 1445–1463, <https://doi.org/10.5194/amt-10-1445-2017>, 2017.
- Edward P. Hunter and Sharon G. Lias: Proton Affinity Evaluation, in: NIST Chemistry WebBook, NIST Standard Reference Database Number 69, Eds. P.J. Linstrom and W.G. Mallard, National Institute of Standards and Technology, Gaithersburg MD, 20899, <https://doi.org/https://doi.org/10.18434/T4D303>.
- 600 Faxon, C., Hammes, J., Le Breton, M., Pathak, R. K., and Hallquist, M.: Characterization of organic nitrate constituents of secondary organic aerosol (SOA) from nitrate-radical-initiated oxidation of limonene using high-resolution chemical ionization mass spectrometry, *Atmospheric Chemistry and Physics*, 18, 5467–5481, <https://doi.org/10.5194/acp-18-5467-2018>, 2018.
- Fry, J. L., Draper, D. C., Zarzana, K. J., Campuzano-Jost, P., Day, D. A., Jimenez, J. L., Brown, S. S., Cohen, R. C., Kaser, L., Hansel, A., Cappellin, L., Karl, T., Hodzic Roux, A., Turnipseed, A., Cantrell, C., Lefer, B. L., and Grossberg, N.: Observations of gas- and aerosol-

- 605 phase organic nitrates at BEACHON-RoMBAS 2011, *Atmospheric Chemistry and Physics*, 13, 8585–8605, <https://doi.org/10.5194/acp-13-8585-2013>, 2013.
- Goldstein, A. and Galbally, I. E.: Known and Unexplored Organic Constituents in the Earth's Atmosphere, *Environmental Science and Technology*, pp. 1515–1520, 2007.
- Gouw, J. D. and Warneke, C.: Measurements of volatile organic compounds in the earth's atmosphere using proton-transfer-reaction mass spectrometry, *Mass Spectrometry Reviews*, 26, 223–257, <https://doi.org/10.1002/mas.20119>, 2007.
- 610 Hansel, A., Scholz, W., Mentler, B., Fischer, L., and Berndt, T.: Detection of RO₂ radicals and other products from cyclohexene ozonolysis with NH₄⁺ and acetate chemical ionization mass spectrometry, *Atmospheric Environment*, 186, 248–255, <https://doi.org/10.1016/j.atmosenv.2018.04.023>, 2018.
- He, X.-C., Shen, J., Iyer, S., Juuti, P., Zhang, J., Koirala, M., Kytökari, M. M., Worsnop, D. R., Rissanen, M., Kulmala, M., Maier, N. M., Mikkilä, J., Sipilä, M., and Kangasluoma, J.: Characterisation of gaseous iodine species detection using the multi-scheme chemical ionisation inlet 2 with bromide and nitrate chemical ionisation methods, *Atmospheric Measurement Techniques*, 16, 4461–4487, <https://doi.org/10.5194/amt-16-4461-2023>, 2023.
- 615 Heald, C. L. and Kroll, J. H.: The fuel of atmospheric chemistry: Toward a complete description of reactive organic carbon, *Science Advances*, 6, <https://doi.org/https://doi.org/10.1126/sciadv.aay8967>, 2020.
- 620 Huey, L. G.: Measurement of trace atmospheric species by chemical ionization mass spectrometry: speciation of reactive nitrogen and future directions, *Mass Spectrom Rev*, 26, 166–84, <https://doi.org/10.1002/mas.20118>, 2007.
- Hunter, E. and Lias, S.: *Evaluated Gas Phase Basicities and Proton Affinities of Molecules: An Update*, 1998.
- Hunter, J. F., Day, D. A., Palm, B. B., Yatavelli, R. L. N., Chan, A. W. H., Kaser, L., Cappellin, L., Hayes, P. L., Cross, E. S., Carrasquillo, A. J., Campuzano-Jost, P., Stark, H., Zhao, Y., Hohaus, T., Smith, J., Hansel, A., Karl, T., Goldstein, A. H., Guenther, A., Worsnop, D., Thornton, J. A., Heald, C. L., Jimenez, J. L., and Kroll, J. H.: Comprehensive characterization of atmospheric organic carbon at a forested site, *Nature Geoscience*, <https://doi.org/10.1038/ngeo3018>, 2017.
- 625 Jenkin, M. E., Young, J. C., and Rickard, A. R.: The MCM v3.3.1 degradation scheme for isoprene, *Atmospheric Chemistry and Physics*, 15, 11 433–11 459, <https://doi.org/10.5194/acp-15-11433-2015>, 2015.
- Jensen, A. R., Koss, A. R., Hales, R. B., and de Gouw, J. A.: Measurements of volatile organic compounds in ambient air by gas-chromatography and real-time Vocus PTR-TOF-MS: calibrations, instrument background corrections, and introducing a PTR Data Toolkit, *Atmospheric Measurement Techniques*, 16, 5261–5285, <https://doi.org/10.5194/amt-16-5261-2023>, 2023.
- 630 Jordan, A., Haidacher, S., Hanel, G., Hartungen, E., Herbig, J., Märk, L., Schottkowsky, R., Seehauser, H., Sulzer, P., and Märk, T. D.: An online ultra-high sensitivity Proton-transfer-reaction mass-spectrometer combined with switchable reagent ion capability (PTR+SRI-MS), *International Journal of Mass Spectrometry*, 286, 32–38, <https://doi.org/10.1016/j.ijms.2009.06.006>, 2009.
- 635 Kari, E., Miettinen, P., Yli-Pirilä, P., Virtanen, A., and Faiola, C. L.: PTR-ToF-MS product ion distributions and humidity-dependence of biogenic volatile organic compounds, *International Journal of Mass Spectrometry*, 430, 87–97, <https://doi.org/10.1016/j.ijms.2018.05.003>, 2018.
- Kaser, L., Karl, T., Guenther, A., Graus, M., Schnitzhofer, R., Turnipseed, A., Fischer, L., Harley, P., Madronich, M., Gochis, D., Keutsch, F. N., and Hansel, A.: Undisturbed and disturbed above canopy ponderosa pine emissions: PTR-TOF-MS measurements and MEGAN 2.1 model results, *Atmospheric Chemistry and Physics*, 13, 11 935–11 947, <https://doi.org/10.5194/acp-13-11935-2013>, 2013.
- 640 Khare, P., Krechmer, J. E., Machesky, J. E., Hass-Mitchell, T., Cao, C., Wang, J., Majluf, F., Lopez-Hilfiker, F., Malek, S., Wang, W., Seltzer, K., Pye, H. O. T., Commane, R., McDonald, B. C., Toledo-Crow, R., Mak, J. E., and Gentner, D. R.: Ammonium-adduct chemical

- ionization to investigate anthropogenic oxygenated gas-phase organic compounds in urban air, *Atmos Chem Phys*, 22, 14 377–14 399, <https://doi.org/10.5194/acp-22-14377-2022>, 2022.
- 645 Kilgour, D. B., Novak, G. A., Sauer, J. S., Moore, A. N., Dinasquet, J., Amiri, S., Franklin, E. B., Mayer, K., Winter, M., Morris, C. K., Price, T., Malfatti, F., Crocker, D. R., Lee, C., Cappa, C. D., Goldstein, A. H., Prather, K. A., and Bertram, T. H.: Marine gas-phase sulfur emissions during an induced phytoplankton bloom, *Atmos Chem Phys*, 22, 1601–1613, <https://doi.org/https://doi.org/10.5194/acp-22-1601-2022>, 2022.
- Kilgour, D. B., Novak, G. A., Claffin, M. S., Lerner, B. M., and Bertram, T. H.: Production of oxygenated volatile organic compounds from
650 the ozonolysis of coastal seawater, *Atmospheric Chemistry and Physics*, 24, 3729–3742, <https://doi.org/10.5194/acp-24-3729-2024>, 2024.
- Kim, M. J., Zoerb, M. C., Campbell, N. R., Zimmermann, K. J., Blomquist, B. W., Huebert, B. J., and Bertram, T. H.: Revisiting benzene cluster cations for the chemical ionization of dimethyl sulfide and select volatile organic compounds, *Atmospheric Measurement Techniques*, 9, 1473–1484, <https://doi.org/10.5194/amt-9-1473-2016>, 2016.
- Krechmer, J., Lopez-Hilfiker, F., Koss, A., Hutterli, M., Stoerner, C., Deming, B., Kimmel, J., Warneke, C., Holzinger, R., Jayne, J., Worsnop,
655 D., Fuhrer, K., Gonin, M., and de Gouw, J.: Evaluation of a New Reagent-Ion Source and Focusing Ion–Molecule Reactor for Use in Proton-Transfer-Reaction Mass Spectrometry, *Analytical Chemistry*, 90, 12 011–12 018, <https://doi.org/10.1021/acs.analchem.8b02641>, 2018.
- Lee, B. H., Lopez-Hilfiker, F. D., Mohr, C., Kurtén, T., Worsnop, D. R., and Thornton, J. A.: An Iodide-Adduct High-Resolution Time-of-Flight Chemical-Ionization Mass Spectrometer: Application to Atmospheric Inorganic and Organic Compounds, *Environmental Science
660 and Technology*, 48, 6309–6317, <https://doi.org/10.1021/es500362a>, 2014.
- Lee, B. H., Lopez-Hilfiker, F. D., Veres, P. R., McDuffie, E. E., Fibiger, D. L., Sparks, T. L., Ebben, C. J., Green, J. R., Schroder, J. C., Campuzano-Jost, P., Iyer, S., D’Ambro, E. L., Schobesberger, S., Brown, S. S., Wooldridge, P. J., Cohen, R. C., Fiddler, M. N., Bililign, S., Jimenez, J. L., Kurtén, T., Weinheimer, A. J., Jaegle, L., and Thornton, J. A.: Flight Deployment of a High-Resolution Time-of-Flight Chemical Ionization Mass Spectrometer: Observations of Reactive Halogen and Nitrogen Oxide Species, *Journal of Geophysical
665 Research: Atmospheres*, <https://doi.org/10.1029/2017jd028082>, 2018.
- Legrand, M., Sciare, J., Jourdain, B., and Genthon, C.: Subdaily variations of atmospheric dimethylsulfide, dimethylsulfoxide, methane-sulfonate, and non-sea-salt sulfate aerosols in the atmospheric boundary layer at Dumont d’Urville (coastal Antarctica) during summer, *Journal of Geophysical Research: Atmospheres*, 106, 14 409–14 422, <https://doi.org/10.1029/2000JD900840>, 2001.
- Li, F., Huang, D. D., Tian, L., Yuan, B., Tan, W., Zhu, L., Ye, P., Worsnop, D., Hoi, K. I., Mok, K. M., and Li, Y. J.: Response of protonated, adduct, and fragmented ions in Vocus proton-transfer-reaction time-of-flight mass spectrometer (PTR-ToF-MS), *Atmospheric
670 Measurement Techniques*, 17, 2415–2427, <https://doi.org/10.5194/amt-17-2415-2024>, 2024.
- Li, H., Canagaratna, M. R., Riva, M., Rantala, P., Zhang, Y., Thomas, S., Heikkinen, L., Flaud, P.-M., Villenave, E., Perraudin, E., Worsnop, D., Kulmala, M., Ehn, M., and Bianchi, F.: Atmospheric organic vapors in two European pine forests measured by a Vocus PTR-TOF: insights into monoterpene and sesquiterpene oxidation processes, *Atmospheric Chemistry and Physics*, 21, 4123–4147, <https://doi.org/10.5194/acp-21-4123-2021>, 2021.
- Link, M. F., Pothier, M. A., Vermeuel, M. P., Riches, M., Millet, D. B., and Farmer, D. K.: In-Canopy Chemistry, Emissions, Deposition, and Surface Reactivity Compete to Drive Bidirectional Forest-Atmosphere Exchange of VOC Oxidation Products, *ACS ES&T Air*, 1, 305–315, <https://doi.org/10.1021/acsestair.3c00074>, 2024.

- McKinney, K. A., Lee, B. H., Vasta, A., Pho, T. V., and Munger, J. W.: Emissions of isoprenoids and oxygenated biogenic volatile organic compounds from a New England mixed forest, *Atmospheric Chemistry and Physics*, 11, 4807–4831, <https://doi.org/10.5194/acp-11-4807-2011>, 2011.
- Michael M. Meot-Ner (Mautner) and Sharon G. Lias: Binding Energies Between Ions and Molecules, and The Thermochemistry of Cluster Ions, in: NIST Chemistry WebBook, NIST Standard Reference Database Number 69, Eds. P.J. Linstrom and W.G. Mallard, National Institute of Standards and Technology, Gaithersburg MD, 20899, <https://doi.org/https://doi.org/10.18434/T4D303>.
- Muller, M., Piel, F., Gutmann, R., Sulzer, P., Hartungen, E., and Wisthaler, A.: A novel method for producing NH₄⁺ reagent ions in the hollow cathode glow discharge ion source of PTR-MS instruments, *International Journal of Mass Spectrometry*, 447, <https://doi.org/10.1016/j.ijms.2019.116254>, 2020.
- Mungall, E. L., Abbatt, J. P. D., Wentzell, J. J. B., Lee, A. K. Y., Thomas, J. L., Blais, M., Gosselin, M., Miller, L. A., Papakyr-
iakou, T., Willis, M. D., and Liggio, J.: Microlayer source of oxygenated volatile organic compounds in the summertime ma-
rine Arctic boundary layer, *Proceedings of the National Academy of Sciences of the United States of America*, 114, 6203–6208,
<https://doi.org/10.1073/pnas.1620571114>, 2017.
- Nah, T., Ji, Y., Tanner, D. J., Guo, H., Sullivan, A. P., Ng, N. L., Weber, R. J., and Huey, L. G.: Real-time measurements of gas-phase organic acids using SF₆- chemical ionization mass spectrometry, *Atmospheric Measurement Techniques*, 11, 5087–5104, <https://doi.org/10.5194/amt-11-5087-2018>, 2018.
- Nowak, J. B., Davis, D. D., Chen, G., Eisele, F. L., Mauldin, R. L., Tanner, D. J., Cantrell, C., Kosciuch, E., Bandy, A., Thornton, D., and Clarke, A.: Airborne observations of DMSO, DMS, and OH at marine tropical latitudes, *Geophysical Research Letters*, 28, 2201–2204, <https://doi.org/10.1029/2000GL012297>, 2001.
- Ortega, J., Turnipseed, A., Guenther, A. B., Karl, T. G., Day, D. A., Gochis, D., Huffman, J. A., Prenni, A. J., Levin, E. J., Kreidenweis, S. M., Demott, P. J., Tobo, Y., Patton, E. G., Hodzic, A., Cui, Y. Y., Harley, P. C., Hornbrook, R. S., Apel, E. C., Monson, R. K.,
Eller, A. S., Greenberg, J. P., Barth, M. C., Campuzano-Jost, P., Palm, B. B., Jimenez, J. L., Aiken, A. C., Dubey, M. K., Geron, C.,
Offenberg, J., Ryan, M. G., Fornwalt, P. J., Pryor, S. C., Keutsch, F. N., Digangi, J. P., Chan, A. W., Goldstein, A. H., Wolfe, G. M.,
Kim, S., Kaser, L., Schnitzhofer, R., Hansel, A., Cantrell, C. A., Mauldin, R. L., and Smith, J. N.: Overview of the Manitou experimental forest observatory: Site description and selected science results from 2008 to 2013, *Atmospheric Chemistry and Physics*, 14, 6345–6367, <https://doi.org/10.5194/ACP-14-6345-2014>, 2014.
- Pagonis, D., Krechmer, J. E., de Gouw, J., Jimenez, J. L., and Ziemann, P. J.: Effects of gas–wall partitioning in Teflon tubing and instrumentation on time-resolved measurements of gas-phase organic compounds, *Atmospheric Measurement Techniques*, 10, 4687–4696, <https://doi.org/10.5194/amt-10-4687-2017>, 2017.
- Pagonis, D., Sekimoto, K., and de Gouw, J.: A Library of Proton-Transfer Reactions of H₃O⁽⁺⁾ Ions Used for Trace Gas Detection, *J Am Soc Mass Spectrom*, 30, 1330–1335, <https://doi.org/10.1007/s13361-019-02209-3>, 2019.
- Putaud, J., Davison, B., Watts, S., Mihalopoulos, N., Nguyen, B., and Hewitt, C.: Dimethylsulfide and its oxidation products at two sites in Brittany (France), *Atmospheric Environment*, 33, 647–659, [https://doi.org/10.1016/S1352-2310\(98\)00104-6](https://doi.org/10.1016/S1352-2310(98)00104-6), 1999.
- Riches, M., Berg, T. C., Vermeuel, M. P., Millet, D. B., and Farmer, D. K.: Wildfire Smoke Directly Changes Biogenic Volatile Organic Emissions and Photosynthesis of Ponderosa Pines, *Geophysical Research Letters*, 51, e2023GL106667, <https://doi.org/10.1029/2023GL106667>, 2024.

- 715 Rissanen, M. P., Mikkilä, J., Iyer, S., and Hakala, J.: Multi-scheme chemical ionization inlet (MION) for fast switching of reagent ion chemistry in atmospheric pressure chemical ionization mass spectrometry (CIMS) applications, *Atmospheric Measurement Techniques*, 12, 6635–6646, <https://doi.org/10.5194/amt-12-6635-2019>, 2019.
- Riva, M., Rantala, P., Krechmer, J. E., Peräkylä, O., Zhang, Y., Heikkinen, L., Garmash, O., Yan, C., Kulmala, M., Worsnop, D., and Ehn, M.: Evaluating the performance of five different chemical ionization techniques for detecting gaseous oxygenated organic species, *Atmospheric Measurement Techniques*, 12, 2403–2421, <https://doi.org/10.5194/amt-12-2403-2019>, 2019.
- 720 Roberts, J. M., Veres, P., Warneke, C., Neuman, J. A., Washenfelder, R. A., Brown, S. S., Baasandorj, M., Burkholder, J. B., Burling, I. R., Johnson, T. J., Yokelson, R. J., and de Gouw, J.: Measurement of HONO, HNCO, and other inorganic acids by negative-ion proton-transfer chemical-ionization mass spectrometry (NI-PT-CIMS): application to biomass burning emissions, *Atmospheric Measurement Techniques*, 3, 981–990, <https://doi.org/10.5194/amt-3-981-2010>, 2010.
- 725 Saunders, S. M., Jenkin, M. E., Derwent, R. G., and Pilling, M. J.: Protocol for the development of the Master Chemical Mechanism, MCM v3 (Part A): tropospheric degradation of non-aromatic volatile organic compounds, *Atmospheric Chemistry and Physics*, 3, 161–180, <https://doi.org/10.5194/acp-3-161-2003>, 2003.
- Sciare, J., Kanakidou, M., and Mihalopoulos, N.: Diurnal and seasonal variation of atmospheric dimethylsulfoxide at Amsterdam Island in the southern Indian Ocean, *Journal of Geophysical Research: Atmospheres*, 105, 17 257–17 265, <https://doi.org/10.1029/1999JD901186>, 2000.
- 730 Smith, D. and Spanel, P.: Selected ion flow tube mass spectrometry (SIFT-MS) for on-line trace gas analysis, *Mass Spectrom Rev*, 24, 661–700, <https://doi.org/10.1002/mas.20033>, 2005.
- Stockwell, C. E., Coggon, M. M., Gkatzelis, G. I., Ortega, J., McDonald, B. C., Peischl, J., Aikin, K., Gilman, J. B., Trainer, M., and Warneke, C.: Volatile organic compound emissions from solvent- and water-borne coatings – compositional differences and tracer compound identifications, *Atmospheric Chemistry and Physics*, 21, 6005–6022, <https://doi.org/10.5194/acp-21-6005-2021>, 2021.
- 735 US EPA: Estimations Programs Interface Suite for Microsoft Windows, <https://www.epa.gov/tsca-screening-tools/epi-suitetm-estimation-program-interface>.
- Vermeuel, M. P., Millet, D. B., Farmer, D. K., Pothier, M. A., Link, M. F., Riches, M., Williams, S., and Garofalo, L. A.: Closing the Reactive Carbon Flux Budget: Observations From Dual Mass Spectrometers Over a Coniferous Forest, *Journal of Geophysical Research: Atmospheres*, 128, e2023JD038 753, <https://doi.org/10.1029/2023JD038753>, 2023a.
- 740 Vermeuel, M. P., Novak, G. A., Kilgour, D. B., Claffin, M. S., Lerner, B. M., Trowbridge, A. M., Thom, J., Cleary, P. A., Desai, A. R., and Bertram, T. H.: Observations of biogenic volatile organic compounds over a mixed temperate forest during the summer to autumn transition, *Atmospheric Chemistry and Physics*, 23, 4123–4148, <https://doi.org/10.5194/acp-23-4123-2023>, 2023b.
- Warneke, C., Van Der Veen, C., Luxembourg, S., De Gouw, J., and Kok, A.: Measurements of benzene and toluene in ambient air using proton-transfer-reaction mass spectrometry: calibration, humidity dependence, and field intercomparison, *International Journal of Mass Spectrometry*, 207, 167–182, [https://doi.org/10.1016/S1387-3806\(01\)00366-9](https://doi.org/10.1016/S1387-3806(01)00366-9), 2001.
- 745 Xu, L., Crounse, J. D., Vasquez, K. T., Allen, H., Wennberg, P. O., Bourgeois, I., Brown, S. S., Campuzano-Jost, P., Coggon, M. M., Crawford, J. H., DiGangi, J. P., Diskin, G. S., Fried, A., Gargulinski, E. M., Gilman, J. B., Gkatzelis, G. I., Guo, H., Hair, J. W., Hall, S. R., Halliday, H. A., Hanisco, T. F., Hannun, R. A., Holmes, C. D., Huey, L. G., Jimenez, J. L., Lamplugh, A., Lee, Y. R., Liao, J., Lindaas, J., Neuman, J. A., Nowak, J. B., Peischl, J., Peterson, D. A., Piel, F., Richter, D., Rickly, P. S., Robinson, M. A., Rollins, A. W., Ryerson, T. B., Sekimoto, K., Selimovic, V., Shingler, T., Soja, A. J., St Clair, J. M., Tanner, D. J., Ullmann, K., Veres, P. R., Walega, J., Warneke, C.,
- 750

- Washenfelder, R. A., Weibring, P., Wisthaler, A., Wolfe, G. M., Womack, C. C., and Yokelson, R. J.: Ozone chemistry in western U.S. wildfire plumes, *Sci Adv*, 7, eabl3648, <https://doi.org/10.1126/sciadv.abl3648>, 2021.
- 755 Xu, L., Coggon, M. M., Stockwell, C. E., Gilman, J. B., Robinson, M. A., Breitenlechner, M., Lamplugh, A., Crounse, J. D., Wennberg, P. O., Neuman, J. A., Novak, G. A., Veres, P. R., Brown, S. S., and Warneke, C.: Chemical ionization mass spectrometry utilizing ammonium ions (NH₄⁺ CIMS) for measurements of organic compounds in the atmosphere, *Atmospheric Measurement Techniques*, 15, 7353–7373, <https://doi.org/10.5194/amt-15-7353-2022>, 2022.
- Yuan, B., Koss, A. R., Warneke, C., Coggon, M., Sekimoto, K., and de Gouw, J. A.: Proton-Transfer-Reaction Mass Spectrometry: Applications in Atmospheric Sciences, *Chem Rev*, 117, 13 187–13 229, <https://doi.org/10.1021/acs.chemrev.7b00325>, 2017.
- 760 Zang, C. and Willis, M.: Replication Data for: Deployment and evaluation of an NH₄⁺ /H₃O⁺ reagent-ion switching chemical ionization mass spectrometer for the detection of reduced and oxygenated gas-phase organic compounds, <https://doi.org/https://doi.org/10.7910/DVN/FL0CZM>, 2024.
- Zaytsev, A., Breitenlechner, M., Koss, A. R., Lim, C. Y., Rowe, J. C., Kroll, J. H., and Keutsch, F. N.: Using collision-induced dissociation to constrain sensitivity of ammonia chemical ionization mass spectrometry (NH₄⁺ CIMS) to oxygenated volatile organic compounds, *Atmos Meas Tech*, 12, 1861–1870, <https://doi.org/10.5194/amt-12-1861-2019>, 2019a.
- 765 Zaytsev, A., Koss, A. R., Breitenlechner, M., Krechmer, J. E., Nihill, K. J., Lim, C. Y., Rowe, J. C., Cox, J. L., Moss, J., Roscioli, J. R., Canagaratna, M. R., Worsnop, D. R., Kroll, J. H., and Keutsch, F. N.: Mechanistic study of the formation of ring-retaining and ring-opening products from the oxidation of aromatic compounds under urban atmospheric conditions, *Atmos Chem Phys*, 19, 15 117–15 129, <https://doi.org/10.5194/acp-19-15117-2019>, 2019b.
- 770 Zhang, Q., Zou, X., Liang, Q., Wang, H., Huang, C., Shen, C., and Chu, Y.: Ammonia-Assisted Proton Transfer Reaction Mass Spectrometry for Detecting Triacetone Triperoxide (TATP) Explosive, *J Am Soc Mass Spectrom*, 30, 501–508, <https://doi.org/10.1007/s13361-018-2108-6>, 2019.
- Zhang, W., Xu, L., and Zhang, H.: Recent advances in mass spectrometry techniques for atmospheric chemistry research on molecular-level, *Mass Spectrometry Reviews*, p. mas.21857, <https://doi.org/10.1002/mas.21857>, 2023.
- 775 Zhao, R., Mungall, E. L., Lee, A. K. Y., Aljawhary, D., and Abbatt, J. P. D.: Aqueous-phase photooxidation of levoglucosan - a mechanistic study using aerosol time-of-flight chemical ionization mass spectrometry (Aerosol ToF-CIMS), *Atmospheric Chemistry and Physics*, 14, 9695–9706, <https://doi.org/10.5194/acp-14-9695-2014>, 2014a.
- Zhao, Y., Hennigan, C. J., May, A. A., Tkacik, D. S., de Gouw, J. A., Gilman, J. B., Kuster, W. C., Borbon, A., and Robinson, A. L.: Intermediate-volatility organic compounds: a large source of secondary organic aerosol, *Environ Sci Technol*, 48, 13 743–50, <https://doi.org/10.1021/es5035188>, 2014b.
- 780 Zhou, S., Rivera-Rios, J. C., Keutsch, F. N., and Abbatt, J. P. D.: Identification of organic hydroperoxides and peroxy acids using atmospheric pressure chemical ionization–tandem mass spectrometry (APCI-MS/MS): application to secondary organic aerosol, *Atmospheric Measurement Techniques*, 11, 3081–3089, <https://doi.org/10.5194/amt-11-3081-2018>, 2018.